ISPRS Journal of Photogrammetry and Remote Sensing 187 (2022) 171–190

Contents lists available at ScienceDirect

ISPRS Journal of Photogrammetry and Remote Sensing

journal homepage: www.elsevier.com/locate/isprsjprs

Fusion of optical, radar and waveform LiDAR observations for land cover classification

Huiran Jin [a], Giorgos Mountrakis [b,*]

[a] School of Applied Engineering and Technology, Newark College of Engineering, New Jersey Institute of Technology, Newark, NJ 07102, USA
[b] Department of Environmental Resources Engineering, State University of New York College of Environmental Science and Forestry, Syracuse, NY 13210, USA

ARTICLE INFO

Keywords:
Fusion
Land cover classification
Optical
SAR
Waveform LiDAR
Accuracy

ABSTRACT

Land cover is an integral component for characterizing anthropogenic activity and promoting sustainable land use. Mapping distribution and coverage of land cover at broad spatiotemporal scales largely relies on classification of remotely sensed data. Although recently multi-source data fusion has been playing an increasingly active role in land cover classification, our intensive review of current studies shows that the integration of optical, synthetic aperture radar (SAR) and light detection and ranging (LiDAR) observations has not been thoroughly evaluated. In this research, we bridged this gap by i) summarizing related fusion studies and assessing their reported accuracy improvements, and ii) conducting our own case study where for the first time fusion of optical, radar and waveform LiDAR observations and the associated improvements in classification accuracy are assessed using data collected by spaceborne or appropriately simulated platforms in the LiDAR case. Multitemporal Landsat-5/Thematic Mapper (TM) and Advanced Land Observing Satellite-1/ Phased Array type L-band SAR (ALOS-1/PALSAR) imagery acquired in the Central New York (CNY) region close to the collection of airborne waveform LVIS (Land, Vegetation, and Ice Sensor) data were examined. Classification was conducted using a random forest algorithm and different feature sets in terms of sensor and seasonality as input variables. Results indicate that the combined spectral, scattering and vertical structural information provided the maximum discriminative capability among different land cover types, giving rise to the highest overall accuracy of 83% (2–19% and 9–35% superior to the two-sensor and single-sensor scenarios with overall accuracies of 64–81% and 48–74%, respectively). Greater improvement was achieved when combining multitemporal Landsat images with LVIS-derived canopy height metrics as opposed to PALSAR features, suggesting that LVIS contributed more useful thematic information complementary to spectral data and beneficial to the classification task, especially for vegetation classes. With the Global Ecosystem Dynamics Investigation (GEDI), a recently launched LiDAR instrument of similar properties to the LVIS sensor now operating onboard the International Space Station (ISS), it is our hope that this research will act as a literature summary and offer guidelines for further applications of multi-date and multi-type remotely sensed data fusion for improved land cover classification.

1. Introduction

Land cover is a fundamental attribute that links physical environments and human activities. As a key determinant of land use, it varies at different spatial scales from local to global and temporal scales from days to millennia (Cihlar, 2000). Timely and accurate information on land cover has been identified as a critical information component for a broad range of environmental and socioeconomic studies and applications, including forest management, desertification control, biodiversity conservation, sustainable land use planning, and climate change monitoring (e.g. Chapin III et al., 2000; Douglas, 1999; Jansen and Gregorio, 2002; Penner, 1994; Skole, 1994; Vitousek, 1994). Knowledge on land cover and the associated dynamics is increasingly required by research scientists, governmental agencies and nonprofit organizations to improve understanding on interactions between the natural landscape and humans and to promote better decision making that will increase socioeconomic welfare while preserving limited land and biodiversity resources.

Remote sensing provides a spatially continuous and highly consistent representation of the Earth's surface (Foody, 2002), and thus has been

* Corresponding author.
E-mail addresses: huiran.jin@njit.edu (H. Jin), gmountrakis@esf.edu (G. Mountrakis).

https://doi.org/10.1016/j.isprsjprs.2022.03.010
Received 9 November 2021; Received in revised form 25 February 2022; Accepted 11 March 2022
Available online 17 March 2022

Table 1
Examples of land cover (and/or land use) classification through multi-type data fusion (published in peer-reviewed journals since 2000).

Authors	Objective(s)	Study site(s)	Sensors			Classification algorithm(s)	Accuracy improved over the use of single-type data
			Optical	SAR	LiDAR		
Adams and Matthews (2018)	Shrubland mapping in a managed forest landscape	Southeastern Ohio, USA	Landsat-8 OLI*		Leica ALS50	Random forest (RF)	9% (OA: overall accuracy)
Adrian et al. (2021)	Crop type mapping	An agricultural site in Columbia, MO, USA	Sentinel-2*	Sentinel-1*		Deep learning (DL)	−4–30% (OA), −0.20–0.21 (Kappa)
Adriano et al. (2019)	Building damage mapping	Palu, Indonesia	Sentinel-2*, PlanetScope	Sentinel-1*, ALOS-2 PALSAR-2*		RF	1–3% (OA)
Alonzo et al. (2014)	Urban tree species mapping	Santa Barbara, CA, USA	AVIRIS		Riegl Q560	Canonical discriminant analysis (CDA)	4–51% (OA)
Amarsaikhan et al. (2010)	Urban land cover classification	Ulaanbaatar, Mongolia	QuickBird	TerraSAR-X		Maximum likelihood (ML)	13% (OA)
Attarchi and Gloaguen (2014)	Mountainous forest classification	Hyrcanian Forest (Loveh), Iran	Landsat-7 ETM+	ALOS-1 PALSAR		ML, RF, support vector machine (SVM), neural network (NN)	−3–12% (OA)
Blaes et al. (2005)	Crop identification	Central Belgium	SPOT XS*, Landsat-7 ETM+	ERS-2*, Radarsat-1*		ML	2–37% (OA)
Bork and Su (2007)	Rangeland vegetation classification	Aspen Parkland, Alberta, Canada	Aerial photos (RGB)#		Optech ALTM2025	ML	16–28% (OA)
Cai et al. (2020)	Wetland mapping	The Dongting Lake wetland, Hunan Province, China	Sentinel-2*, MODIS*	Sentinel-1*		Stacked generalization	7% (OA), 0.05 (Kappa)
Cho et al. (2012)	Savanna tree species mapping	Kruger National Park, South Africa	HiFIS		Small-footprint LiDAR#	ML	3–6% (OA)
Chust et al. (2004)	Mediterranean land cover discrimination	Minorca Island, Spain	SPOT XS*	ERS-1/2*		ML	0.01–0.08 (Kappa)
Dalponte et al. (2008)	Classification of complex forest areas	Bosco della Fontana Natural Reserve, Italy	AISA Eagle		Optech ALTM3100	SVM, ML, *k*-nearest neighbor	0.01–0.05 (Kappa)
Dalponte et al. (2012)	Tree species classification over a mountain area	Southeastern Trento, Italy	AISA Eagle, GeoEye-1		Optech ALTM3100EA	SVM, RF	8–11% (OA), 0.11–0.14 (Kappa)
Du et al. (2021)	Land cover classification	Trento, Italy and University of Southern Mississippi Gulf Park campus, MS, USA and University of Houston campus, TX, USA	Hyperspectral imagery#		LiDAR-derived elevation#	DL	1–2% (OA)
Fagan et al. (2018)	Pine plantation mapping	Southeastern U.S.	Landsat-5 TM*		Riegl VQ-480	Decision tree (DT)	2–5% (OA)
Feng et al. (2019a)	Coastal land cover classification	Yellow River Delta, China	Sentinel-2*	Sentinel-1*		DL	3–30% (OA), 0.04–0.34 (Kappa)
Feng et al. (2019b)+	Urban land use mapping	University of Houston campus, TX, USA	Hyperspectral imagery#		LiDAR-derived DSM#	DL	8–38% (OA), 0.09–0.42 (Kappa)
Forzieri et al. (2013)	Fine-scale mapping of heterogeneous urban/rural landscapes	Marecchia River, Italy	ADS40, MIVIS		LiDAR-derived DTM and DSM#	ML, spectral angle mapper (SAM), spectral information divergence (SID)	5–18% (OA)
Fu et al. (2017)	Wetland vegetation mapping	Sanjiang Plain, China	Gaofen-1	ALOS-1 PALSAR, Radarsat-2		RF	−7–37% (OA), −0.08–0.50 (Kappa)
Furtado et al. (2015)	Land cover classification of the Amazon várzea	The Lago Grande de Curuai floodplain, Pará, Brazil	Landsat-5 TM	Radarsat-2		DT	1–17% (OA), 0.01–0.11 (Kappa)
Geerling et al. (2007)	Floodplain vegetation classification	A floodplain along the river Waal, Netherlands	CASI		Optech ALTM2033	ML	6–27% (OA), 0.06–0.28 (Kappa)
Ghamisi et al. (2017)	Classification of urban/rural landscapes	University of Houston campus, TX, USA and Trento, Italy	CASI, AISA Eagle		LiDAR-derived DSM#, Optech ALTM 3100EA	RF, DL	3–29% (OA), 0.03–0.32 (Kappa)
Guo et al. (2011)	Urban scene classification	Biberach, Germany	Applanix DSS 22 M (RGB)		Riegl LMS-Q560	RF	2–14% (OA)
Hartling et al. (2019)	Urban tree species classification	Forest Park, St. Louis, MO, USA	WorldView-2/3		LiDAR-derived DTM, DSM and intensity#	DL, SVM, RF	3–4% (OA), 0.03–0.05 (Kappa)
	Urban classification		CASI-1500			SVM	

(*continued on next page*)

Table 1 (*continued*)

Authors	Objective(s)	Study site(s)	Sensors			Classification algorithm(s)	Accuracy improved over the use of single-type data
			Optical	SAR	LiDAR		
Hasani et al. (2017)		University of Houston campus, TX, USA			LiDAR-derived DSM[#]		6–14% (OA), 0.07–0.16 (Kappa)
Heckel et al. (2020)	Forest cover delineation	Thuringia, Germany and southern Kruger National Park, South Africa	Sentinel-2A	Sentinel-1A [*]		RF	0–8% (OA)
Held et al. (2003)	Tropical mangrove mapping	The Daintree River estuary, Queensland, Australia	CASI	AIRSAR		ML	6–19% (OA)
Hong et al. (2022)	Classification	Houston, TX, USA and Trento, Italy	Hyperspectral imagery[#]		LiDAR-derived imagery[#]	DL	8–25% (OA), 0.09–0.30 (Kappa)
Hong et al. (2021)	Classification	[1]University of Houston campus, TX, USA [2]Berlin, Germany and Hong Kong, China	[1]CASI-1500 [2]Sentinel-2	[2]Sentinel-1	[1]LiDAR-derived imagery[#]	DL	[1]9–26% (OA), 0.10–0.28 (Kappa) [2]12–23% (OA), 0.11–0.43 (Kappa)
Hribljan et al. (2017)	Tropical mountain peatland mapping and soil carbon storage estimation	Ecuadorian Andes	Landsat-5 TM[*]	ALOS-1 PALSAR[*], Radarsat-1[*]		RF	4–29% (OA)
Huang et al. (2007)	Land cover classification	St. Louis, MO, USA	Landsat-7 ETM+[*]	Radarsat-1		ML	1–10% (OA)
Hütt et al. (2016)[+]	Land use/land cover and crop classification	Sanjiang Plain, China	Formosat-2	TerraSAR-X [*]		ML, RF	2–16% (OA), 0.03–0.21 (Kappa)
Ienco et al. (2019)	Land cover mapping	Reunion Island, France and Koumbia, Tuy, Burkina Faso	Sentinel-2[*]	Sentinel-1[*]		DL	6–16% (OA), 0.07–0.19 (Kappa)
Iervolino et al. (2019)	Classification of a semiarid landscape	Maspalomas Special Natural Reserve, Spain	WorldView-2	TerraSAR-X		ML	2% (OA), 0.04 (Kappa)
Inglada et al. (2016)	Early crop type identification	Toulouse, France	Landsat-8 OLI[*]	Sentinel-1A [*]		RF	0.01–0.10 (Kappa)
Jones et al. (2010)	Coastal tree species mapping	Gulf Islands National Park Reserve, British Columbia, Canada	AISA Dual Eagle + Hawk		TRSI Mark II	SVM	1% (OA), 0 (Kappa)
Ke et al. (2010)	Forest species classification	Heiberg Memorial Forest, NY, USA	QuickBird		Leica ALS50	DT	0.01–0.19 (Kappa)
Koetz et al. (2008)	Land cover classification for forest fire management	Aix-en-Provence, France	AISA Eagle		Optech ALTM3100	SVM	6–44% (OA), 0.07–0.49 (Kappa)
Kuplich et al. (2000)[+]	Land use classification	Campinas, São Paulo State, Brazil	Landsat-5 TM	ERS-1[*]		ML	3–45% (OA)
Kwan et al. (2020a, 2020b)	Land cover classification	University of Houston campus, TX, USA	Hyperspectral imagery[#]		LiDAR-derived elevation[#]	Joint sparse representation (JSR), SVM, DL	−2–6% (OA), −0.02–0.07 (Kappa)
Laurin et al. (2013)	Tropical forest and land cover mapping	Border of Sierra Leone and Liberia	Landsat-5 TM, ALOS-1 AVNIR-2	ALOS-1 PALSAR[*]		ML, NN	2–34% (OA), 0.03–0.39 (Kappa)
Lee and Shan (2003)	Coastal zone mapping	Coastal Camp Lejeune, NC, USA	IKONOS		NASA Airborne Topographic Mapper	ML	1–2% (OA)
Li et al. (2019)	Land cover mapping	University of Houston campus, TX, USA and Rochester, NH, USA	Hyperspectral imagery[#], Headwall Hyperspec Imaging Spectrometer		LiDAR-derived DSM[#], Riegl VQ-480	SVM	3–29% (OA), 0.05–0.31 (Kappa)
Liao et al. (2018)	Tree species mapping	Wijnendale Forest, Belgium	Airborne Prism EXperiment (APEX)		TopoSys Harrier 56	SVM, DL	4–25% (OA), 0.05–0.33 (Kappa)
Liu et al. (2017)	Urban tree species mapping	City of Surrey, British Columbia, Canada	CASI-1500		Leica ALS70-HP [*]	RF	9–19% (OA), 0.10–0.20 (Kappa)
Lu et al. (2011)	Tropical land cover classification	City of Altamira, Brazil	Landsat-5 TM	ALOS-1 PALSAR, Radarsat-2		ML	0–54% (OA), −0.01–0.60 (Kappa)
Luo et al. (2016)	Land cover classification	Zhangye, Gansu Province, China	CASI-1500		Leica ALS70	ML, SVM	8–68% (OA), 0.13–0.71 (Kappa)
McNairn et al. (2009)	Operational annual crop inventory	Five pilot sites across southern Canada	SPOT-4/5[*], Landsat-5 TM[*]	Radarsat-1[*], Envisat ASAR[*]		DT	1–16% (OA), 0–0.23 (Kappa)

(*continued on next page*)

Table 1 (*continued*)

Authors	Objective(s)	Study site(s)	Sensors			Classification algorithm(s)	Accuracy improved over the use of single-type data
			Optical	SAR	LiDAR		
Michelson et al. (2000)	Swedish land cover classification	The Genevad River basin, Sweden	Landsat-5 TM	ERS-1*		ML, sequential maximum *a posteriori* (SMAP), NN	6–20% (OA), 0.07–0.19 (Kappa)
Naidoo et al. (2012)	Savanna tree species classification	The Greater Kruger National Park, South Africa	CASI-1500		Waveform LiDAR#	RF	7–56% (OA), 0.09–0.66 (Kappa)
Park et al. (2018)	Paddy rice mapping	Sutter County, CA, USA and Dangjin, South Korea	Landsat-5 TM*	ALOS-1 PALSAR*, Radarsat-1*		RF, SVM	−1–17% (OA), −0.02–0.24 (Kappa)
Rasti and Ghamisi (2020)	Land cover classification	University of Houston campus, TX, USA and Trento, Italy	ITRES CASI-1500, AISA Eagle		Optech Titam MW, Optech ALTM 3100EA	RF	12–54% (OA), 0.14–0.67 (Kappa)
Reiche et al. (2015)	Detection of tropical deforestation	Viti Levu, Fiji	Landsat-7 ETM+*	ALOS-1 PALSAR*		Break detection For Additive Season and Trend (BFAST)	2–3% (OA)
Sanli et al. (2009)+	Monitoring of land use change and its environmental impacts	Edremit, Turkey	Landsat-5 TM	Radarsat-1		ML	6% (OA), 0.05 (Kappa)
Sasaki et al. (2012)	Land cover and tree species classification	Expo'70 Commemorative Park, Suita, Osaka, Japan	Aerial photos (green, red, near-infrared)#		Optech ALTM2050	ML, DT	3–29% (OA), 0.07–0.39 (Kappa)
Shupe and Marsh (2004)	Desert vegetation mapping	Yuma Proving Ground, AZ, USA	Landsat-5 TM	ERS-1		ML	15–50% (OA), 0.16–0.53 (Kappa)
Singh et al. (2012)	Urban land cover assessment	Mecklenburg County, NC, USA	Landsat-5 TM		Leica ALS50	ML, DT	6–32% (OA)
Sławik et al. (2019)	Vegetation mapping	The lower Biebrza basin, Poland	HySpex (VNIR-1800, SWIR-384)*		Riegl LMS*	RF	0.02–0.11 (Kappa)
Song et al. (2020)	Classification	University of Houston campus, TX, USA	Hyperspectral imagery#		LiDAR-derived DSM#	SVM, extreme learning machine (ELM), DL	1–5% (OA), 0.02–0.05 (Kappa)
Stramondo et al. (2006)	Earthquake damage detection	Izmit, Turkey and Bam, Iran	IRS-1C*, Terra ASTER*	ERS-1/2*, Envisat ASAR*		ML	5–27% (OA), 0.08–0.35 (Kappa)
Sukawattanavijit et al. (2017)	Land cover classification	Central Thailand	Landsat-8 OLI, THEOS	Radarsat-2		SVM	7–14% (OA), 0.16–0.24 (Kappa)
Sun et al. (2019)	Subtropical crop-type mapping	The lower reaches of the Yangzi River, China	Sentinel-2A/B*, Landsat-8 OLI*	Sentinel-1A *		RF, SVM, NN	0–17% (OA), 0.01–0.22 (Kappa)
Teo and Huang (2016)	Land cover classification	Chiayi and Kaohsiung Counties, Taiwan	WorldView-2, CASI-1500		Optech ALTM Pegasus	Nearest neighbor	6–25% (OA), 0.02–0.30 (Kappa)
Torbick et al. (2017)	Rice monitoring	Myanmar	Landsat-8 OLI	Sentinel-1A *, ALOS-2 PALSAR-2		DT	0.01–0.24 (Kappa)
Töyrä et al. (2001)	Wetland flood mapping	Peace-Athabasca Delta, Alberta, Canada	SPOT-4*	Radarsat-1*		Mahalanobis distance	0.12–0.17 (Kappa)
Voss and Sugumaran (2008)	Urban tree species classification	University of Northern Iowa campus, IA, USA	AISA, AISA Eagle		Leica ALS50	Nearest neighbor	9–11% (OA)
Waske and Benediktsson (2007)	Land cover classification	Bonn, Germany	SPOT-5, Landsat-5 TM	Envisat ASAR*, ERS-2*		ML, DT, SVM	0–23% (OA)
Waske and van der Linden (2008)	Land cover classification	Bonn, Germany	Landsat-5 TM	Envisat ASAR*, ERS-2*		SVM, RF	4–7% (OA)
Xu et al. (2018a)	Classification of urban/rural landscapes	University of Houston campus, TX, USA and Trento, Italy	Hyperspectral imagery#		LiDAR-derived DSM#	SVM, ELM, DL	1–34% (OA), 0.02–0.36 (Kappa)
Xu et al. (2018b)	Land cover classification	Williamson County, IL, USA	Landsat-5 TM*		LiDAR-derived occupancy and intensity#	DL	8% (OA), 0.12 (Kappa)
Zhang et al. (2014)	Urban land cover and impervious surface mapping	Pearl River Delta (Guangzhou, Shenzhen, Hong Kong), China	Landsat-7 ETM+, SPOT-5	Envisat-ASAR, TerraSAR-X		RF	1–3% (OA), 0.01–0.03 (Kappa)
Zhou et al. (2018)	Urban land cover classification	Suzhou, Jiangsu Province, China	Landsat-8 OLI, EO-1 Hyperion	Sentinel-1A *		RF	1–6% (OA), 0.01–0.08 (Kappa)
Zhu and Tateishi (2006)	Land cover mapping	Zhangwu County, Liaoning, China	Landsat-5 TM*	ERS-1*		ML, multisensor temporal fusion	0–50% (OA)

(*continued on next page*)

Table 1 (*continued*)

Authors	Objective(s)	Study site(s)	Sensors			Classification algorithm(s)	Accuracy improved over the use of single-type data
			Optical	SAR	LiDAR		
Zhu et al. (2012)	Urban and *peri*-urban land cover classification	Eastern Massachusetts, USA	Landsat-7 ETM+*	ALOS-1 PALSAR		classification (MTFC) RF	1–22% (OA)

* Data acquired at multiple time steps.
# Sensor name not specified.
+ Studies with land use mapping or change monitoring as the claimed objective.

recognized as a major data source for mapping land cover distribution. Optical, synthetic aperture radar (SAR) and light detection and ranging (LiDAR) are three widely adopted remote sensing imaging techniques that use different wavelengths, energy sources and mechanisms, and data acquired encapsulate different information contents. Specifically, optical data provide spectral reflectance measurement of the target illuminated by sunlight, whereas LiDAR returns can characterize the 3-D structure and radar signals are sensitive to the structural and dielectric properties of the target (e.g. roughness and moisture). Although each has been proven useful in numerous classification studies, data fusion

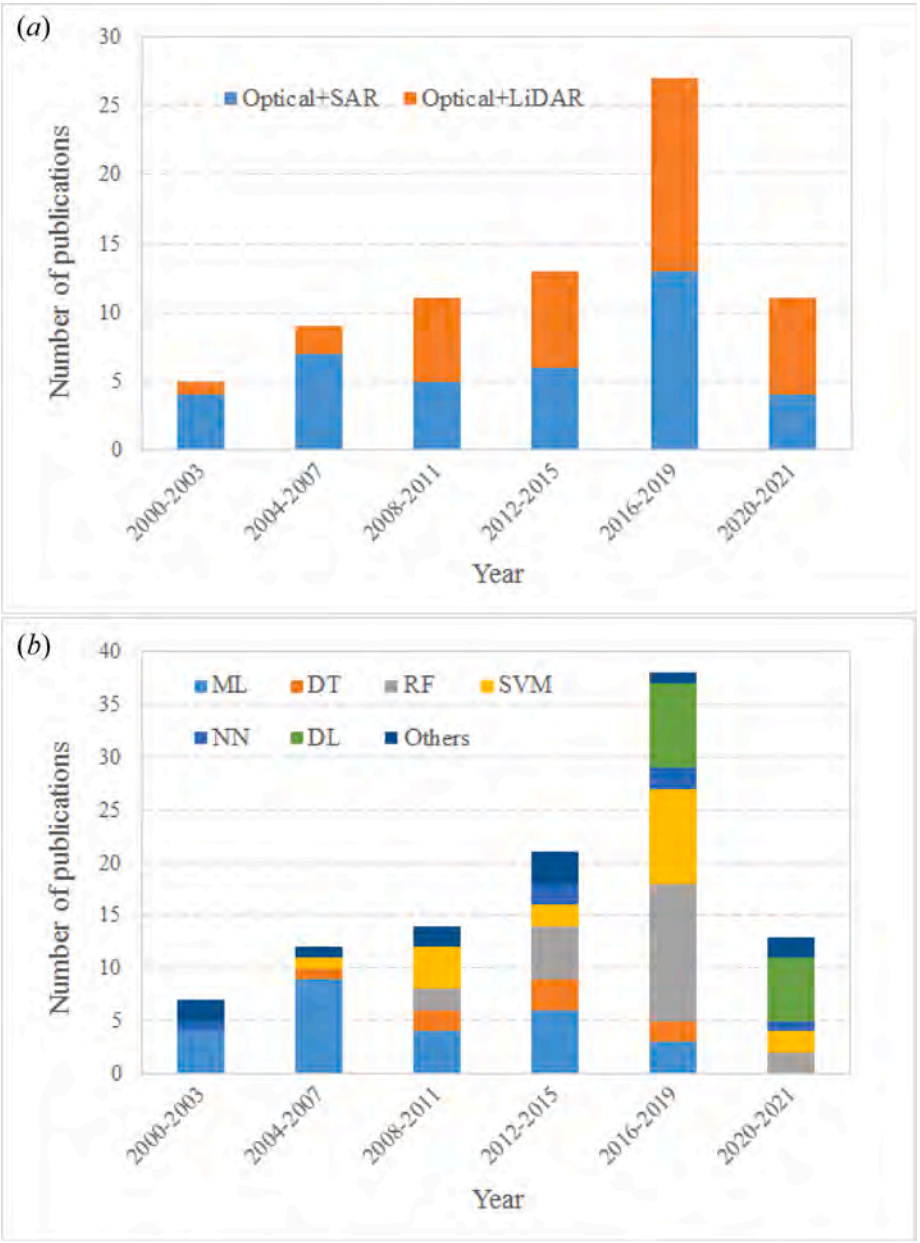

Fig. 1. Growth of classification research over the past two decades based on (*a*) optical–SAR and optical–LiDAR fusion, and (*b*) algorithms applied.

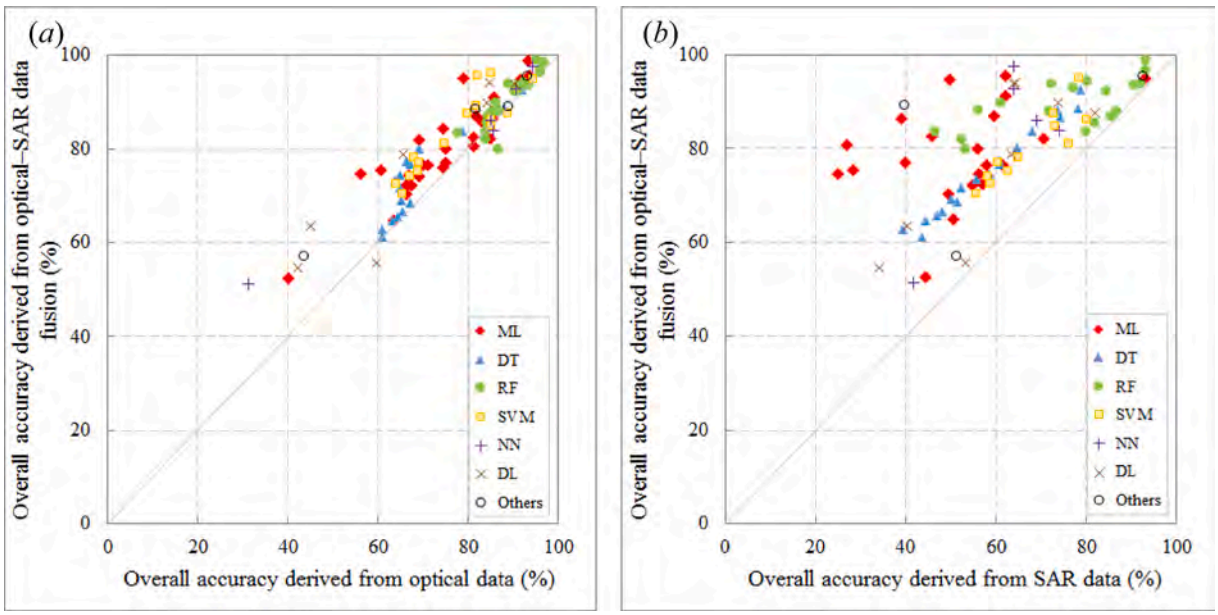

Fig. 2. Comparative performance of (*a*) optical vs. optical–SAR classification, and (*b*) SAR vs. optical–SAR classification.

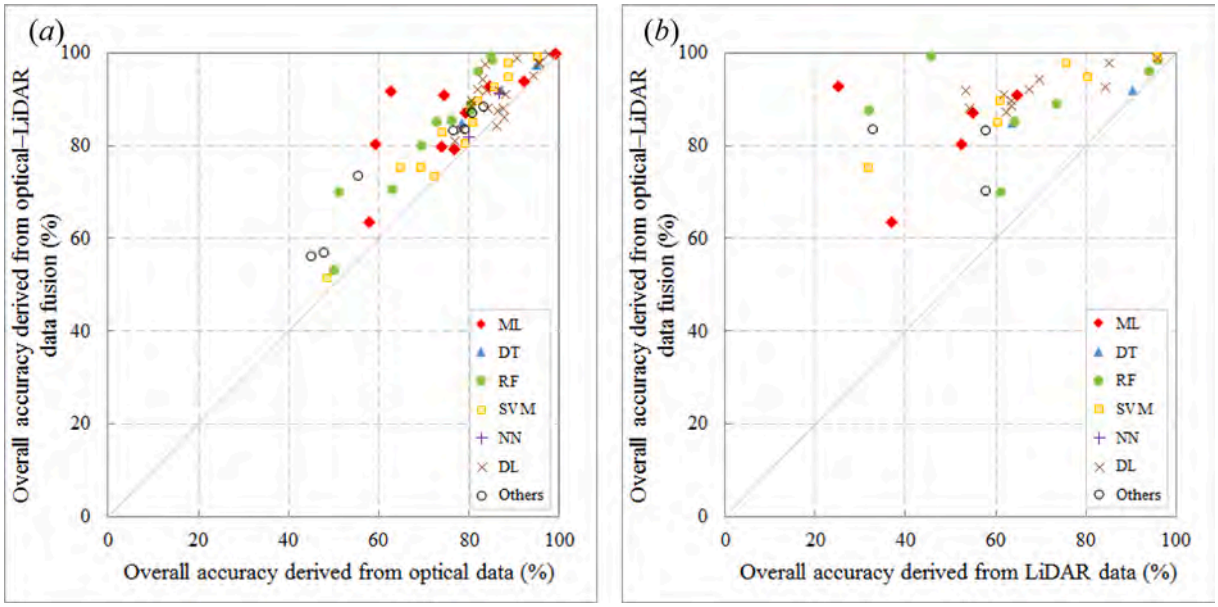

Fig. 3. Comparative performance of (*a*) optical vs. optical–LiDAR classification, and (*b*) LiDAR vs. optical–LiDAR classification.

strategies can combine the complementary information contained in different types of data and contribute to an improved discriminative capability among different land cover classes relative to the use of individual data types. In the past two decades, synergies of multiple data sources for land cover classification have received more and more attention, largely because spaceborne optical and SAR data from operational and archival satellite missions are increasingly available and airborne LiDAR technologies continue to become more mature and affordable.

Table 1 provides a detailed review of existing literature that explored pixel- or feature-level fusion of multi-source data collected by different types of sensors and were published in peer-reviewed journals from 2000 until Oct 2021. These studies were selected as they aimed at mapping land cover (and/or land use) distribution in a wide range of environments from urban, desert and coastal zones, to forest, cropland and rangeland, and most importantly, they explicitly presented classification accuracies from which improvement gained by the fusion could be assessed, a major difference compared to existing reviews of data fusion that are approach oriented (e.g. Ghassemian, 2016; Ghamisi et al., 2019). Among the 75 identified studies, 38 of them examined the combined use of optical and spaceborne SAR images, 36 were based on integration of optical and airborne LiDAR data, and Hong et al. (2021) proposed a multimodal framework and tested it on a hyperspectral-LiDAR dataset and a multispectral-SAR dataset. Over 40% of these studies were developed based on the use of multitemporal data (denoted by a superscript '*') that provide increased information over that from a single date. Also, according to Table 1, marginal to substantial increases in overall accuracy and Kappa were achieved relative to the use of single-type data. A more obvious increasing trend over time can be observed for optical-LiDAR fusion studies (Fig. 1a). With the advent of big data and in parallel with the rapid computational advances, deep learning, a specialized subset of machine learning and a fastest-growing

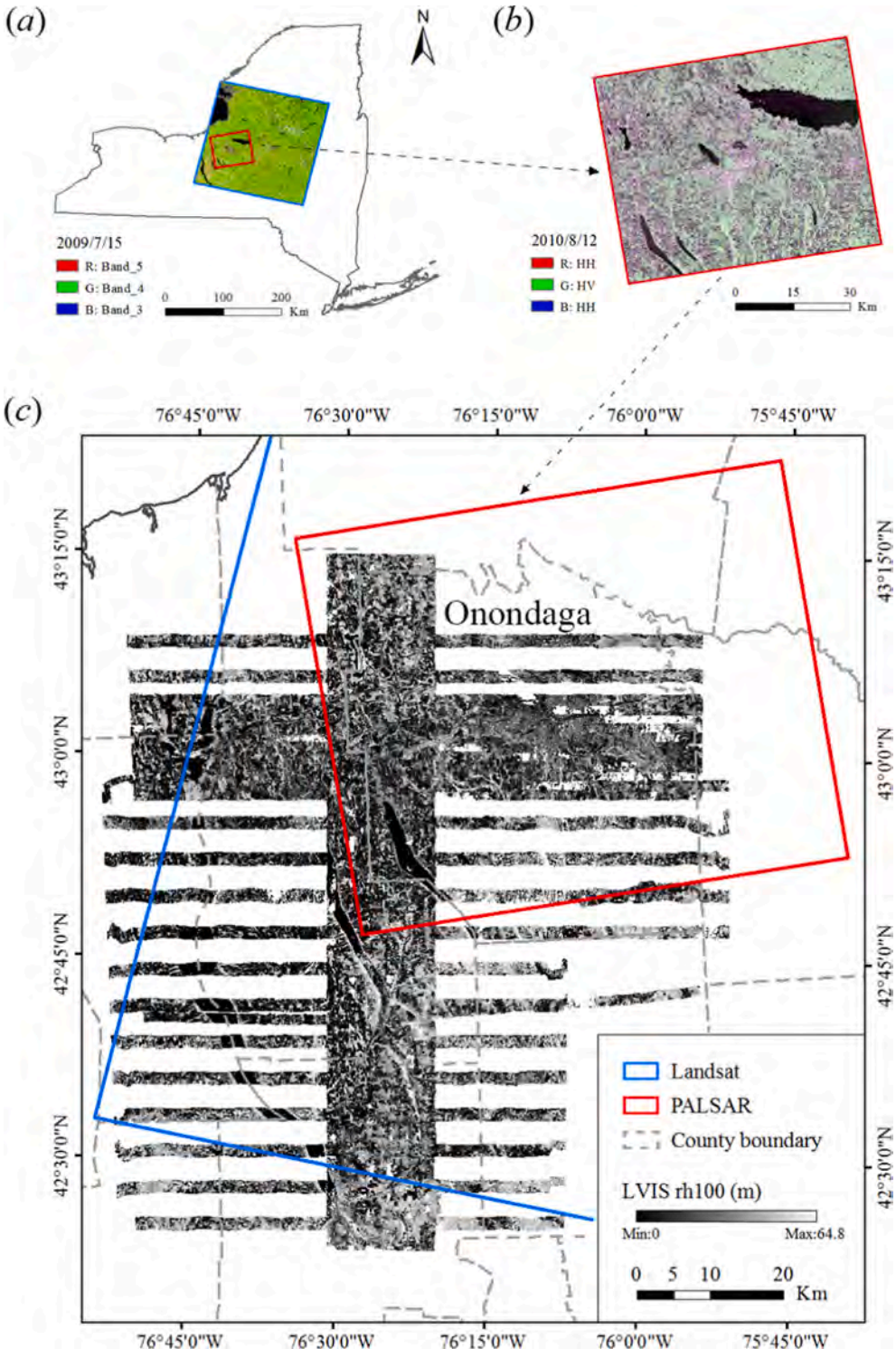

Fig. 4. Image footprints of (*a*) Landsat (path 15, row 30), (*b*) PALSAR (path 134, frame 850), and (*c*) gridded LVIS rh100 over the study area in the CNY region. All classification tasks were conducted over the overlapping area of Landsat, PALSAR and LVIS LiDAR footprints.

trend in data sciences, has gained increasing interest in remote sensing image classification (Fig. 1b).

Regardless of the choice of classification algorithms, more considerable improvements with larger variabilities were always associated with pairwise comparisons of SAR vs. optical-SAR classification (Fig. 2b), and LiDAR vs. optical-LiDAR classification (Fig. 3b), as opposed to optical vs. optical-SAR or optical-LiDAR classification (Fig. 2a and 3a). Only in rare cases did the fusion of optical and SAR data end up with slightly lower accuracies than those derived from optical data alone (shown as points located below the 1:1 line in Fig. 2a). While van Beijma et al. (2014) combined a LiDAR-derived digital surface model (DSM) with aerial photography and airborne SAR data to delineate salt marsh vegetation habitats in the Loughor Estuary, South Wales, UK, and Jahncke et al. (2018) demonstrated the value of incorporating QuickBird optical, LiDAR, and Radarsat-2 full polarimetric SAR data for improved mapping of a wetland area south of Halifax, Nova Scotia,

Table 2
Summary of the data and features used for classification.

Sensor	Spatial resolution (m)	Date	Features*	Number of features
Landsat-5/ TM	30	2009/4/10 (leaf-off) 2009/5/122009/ 7/15 (leaf-on) 2009/10/19	Surface reflectance (SR) and 3 × 3 neighborhood variance at bands 1–5, 7, and the Normalized Difference Vegetation Index (NDVI).	52
ALOS-1/ PALSAR	9.37 (slant range), 3.17–3.20 (azimuth)	2010/5/12 2010/6/272010/ 8/12 (leaf-on)2010/ 11/12 (leaf-off)	Features of intensity, polarimetry, interferometry and texture.	132
LVIS	20 (nominal footprint diameter)	2009/8/ 24–2009/8/26	rh25, rh50, rh75, and rh100.	4

* See Section 3.1 for detailed descriptions of the features extracted from each dataset.

Canada, the synergistic use of all three types of data in classification of more general land cover types and how classification accuracy will be affected have not been thoroughly evaluated.

In addition to providing a summary of recent works and associated improvements, we present here a case study to investigate further the benefits of fusion. Specifically, we aim to address two previously unanswered questions: i) can classification accuracy be improved by combining the three different types of data with a commonly used classifier (random forest), and ii) to what degree the inclusion of seasonal spectral and scattering variations of certain vegetation classes may impact the accuracy when optical, SAR, and LiDAR data are used in combination. Our particular interest is to assess the improvement in classification accuracy attributed to the fusion and the gain of information (as opposed to other factors such as the use of different classifiers). To the best of our knowledge, this is the first work that simultaneously fuses optical, radar and waveform LiDAR observations, where data are acquired from spaceborne or appropriately simulated platforms in the LiDAR case.

The Central New York (CNY) region, which is recognized for its persistent cloudiness and precipitation, was chosen as the study area. Multitemporal Landsat-5/TM and ALOS-1/PALSAR images acquired close to the collection of airborne waveform LiDAR data by NASA's Land, Vegetation, and Ice Sensor (LVIS) were examined. Experiments started from the use of single-date features solely derived from one specific sensor and gradually shifted to multi-date and multi-sensor fusion. Results were analyzed both qualitatively and quantitatively, providing a rare glimpse of the variability of classification performance due to the use of different features as inputs. This research was built upon our earlier work that focused on the integration of multi-type SAR features in vegetation and land cover mapping (Jin et al., 2014), and it is particularly timely now that a spaceborne LiDAR sensor, the Global Ecosystem Dynamics Investigation (GEDI), with similar properties to our examined LVIS sensor is currently operational at the International Space Station.

2. Study area and data

2.1. Study area

The study area is located in the Central New York (CNY) region, mainly in Onondaga County, with a ground extent of approximately 57 km × 52 km (Fig. 4). While our work was evaluated on a single site, it is easily generalizable as the site is sufficiently diverse containing urban and suburban environments, strong water, agriculture and different forest presence and has strong topographic effects. Topography varies substantially in the N-S direction from a fairly level plain of Lake Ontario on the north to high hills in the Appalachian Plateau on the south. The City of Syracuse is located at the center. It receives significant lake-effect snow from Lake Ontario and is considered the snowiest metropolitan city in the United States.

Forests in this region are predominantly second-growth, as intensive agricultural activities led to a major disturbance in the 19th century (Stanton and Bills, 1996). Various deciduous and evergreen species exist, with the ages ranging from 20 to 100 or more years (Zhuang et al., 2015). Common tree species include American beech (*Fagus grandifolia*), sugar maple (*Acer saccharum*), white ash (*Fraxinus americana*), and basswood (*Tilia americana*) as deciduous, and Norway spruce (Picea abies), white pine (Pinus strobus), and eastern hemlock (*Tsuga canadensis*) as evergreen (Nyland et al., 1986). Shrubland as early successional habitats dominated by sparse-to-dense shrubs and intermixed with young trees have moderate presence. Agriculture contributes significantly to the local economy, as farmlands cover more than 30% of total land area in Onondaga County (USDA, 2014). Natural and semi-natural herbaceous plants are mostly in the abandoned farmlands. Such areas have minimal footprints, and thus are merged with agricultural croplands and pasturelands to form a class named herbaceous/ planted. Water, developed and barren lands are also present in the study area. Definitions of all land cover classes assessed are consistent with those applied to the National Land Cover Database (NLCD) series.

2.2. Airborne LiDAR data

LVIS is an airborne, medium footprint, full waveform laser altimeter designed, developed and operated by NASA's Goddard Space Flight Center (GSFC) (Blair et al., 1999). LVIS emits laser pulses at 1064-nm wavelength with 5-mJ output energy and 10-ns bursts. The digitally recorded signals establish a vertical profile of the footprint instantaneously illuminated, from which attributes such as surface topography and vegetation coverage can be derived.

The LVIS data of the study area were acquired by 27 horizontal and 11 vertical flight lines during leaf-on season on August 24–26, 2009. The swath width was approximately 2 km and the nominal footprint diameter was 20 m. The footprint density varied spatially due to swath overlap between adjacent flight lines. Among the standard LVIS products processed at GSFC, the LVIS Ground Elevation (LGE) data were adopted, including geolocation (lat./long.), surface elevation, and relative heights to surface at quartile cumulative return energy (Blair et al., 2006). These height metrics, derived from a Gaussian decomposition algorithm (Hofton et al., 2000), are referred as rh25, rh50, rh75 and rh100 and directly depict the vertical profile of canopy structure (Sun et al., 2011).

Table 3
Training and validation sample sets.

Class	Training	Validation: Number of total (mixed) pixels
Deciduous	200	251 (126)
Evergreen	200	129 (82)
Shrubland	200	124 (66)
Herbaceous/Planted	200	178 (72)
Water	200	130 (34)
Developed	200	129 (35)
Barren	200	159 (13)
Total	1,400	1,100 (428)

2.3. Satellite optical and SAR data

Optical data were represented by four images acquired by Landsat-5/TM and SAR data were comprised of four images from ALOS-1/PALSAR. All image dates were within 1–2 years of the LVIS campaign. Considering the high stability of the study area, no significant errors were introduced by this small temporal variability. Both the spectral and the radar datasets included one image in the leaf-on season, one image in the leaf-off season, and two images during the transitional period between leaf-on and leaf-off conditions (Table 2).

The selected Landsat scenes at path 15/row 30 (UTM Zone 18 North, WGS-84) had minimal cloud and cloud shadow contamination over the study area. All were obtained from the USGS Earth Resources Observation and Science (EROS) Center (source: https://earthexplorer.usgs.gov) and processed to Level 1 T through Standard Terrain Correction. The six reflective bands (1–5 and 7) at the 30 m spatial resolution were extracted to provide spectral information of different land cover types.

Single look complex (SLC) PALSAR Level 1.1 data in the fine beam dual (FBD) polarization (HH and HV) mode were downloaded from the Alaska Satellite Facility Distributed Active Archive Center (ASF-DAAC, source: https://asf.alaska.edu), all from an off-nadir angle of 34.3 degrees in an ascending orbit at path 134/frame 850. Slant range pixel spacing is 9.37 m, and azimuth pixel spacing is 3.17–3.20 m. Meteorological data collected at a weather station in the City of Syracuse showed that cumulative precipitation was less than 4 mm within 24 h prior to the dates of PALSAR acquisition and there was no snow on the ground at the time of PALSAR overpass (Jin et al., 2014).

3. Methodology

The procedure implemented for land cover classification can be summarized as follows. Multiple features were first derived from the co-registered Landsat, PALSAR and LVIS data, respectively (Table 2). A set of thematic maps was then produced using the same training sample set extracted from high-resolution orthoimagery but different combinations of the features as classification inputs. The quality of the maps was evaluated on an independent validation sample set in terms of classification accuracy. Finally, importance of three feature sets, each corresponding to a specific sensor, was analyzed with respect to individual and all land cover types assessed in this study.

3.1. Feature extraction

For each Landsat-5/TM scene, digital numbers (DNs) of bands 1–5 and 7 were converted to surface reflectance (SR) using the Landsat Ecosystem Disturbance Adaptive Processing System (LEDAPS) algorithm (Masek et al., 2006), exactly the one that has been applied to generate the official Landsat TM and ETM + Level 2 SR products (USGS, 2020a, 2020b). To avoid the high correlation among the numerous indices that have been proposed, a single but frequently used metric was extracted from the spatial and spectral domain, respectively. Specifically, variance was computed on each SR band using a 3 × 3 moving window to express the spatial correlation (or variability) of neighboring pixels, and the Normalized Difference Vegetation Index (NDVI) was derived from SR of the near-infrared and red bands as a major indicator of the presence, density and health of vegetation (Tucker, 1979). We also avoided removing potentially correlated variables to allow the classifier to reach its full potential. Therefore, the total number of features per scene was 13 comprised of the SR and variance of each of the six reflective bands and the NDVI.

Features extracted from multitemporal ALOS-1/PALSAR data can be summarized into four categories, namely intensity, polarimetry, interferometry and texture. Intensity metrics characterize the strength of the radar signals returned and detected by the sensor. Polarimetric parameters obtained through decomposition approaches describe the type and contribution of different scattering mechanisms (i.e. surface, double bounce, and volume scattering). Interferometric coherence quantifies the degree of similarity and to which the target area remains unchanged at two separate times. Spatial texture measures the spatial pattern of ground objects from various aspects (e.g. smoothness, variation, dependency). Detailed descriptions of PALSAR data processing and feature extraction are provided in Jin et al. (2014). To facilitate a direct overlay, all PALSAR-derived features were co-registered to Landsat scenes using a collection of 24 ground control points (GCPs) on screen, and resampled to 30 m pixel size through a bilinear interpolation. This is consistent with the routine and commonly adopted protocol for image-to-image registration, and a total root mean square (RMS) error of less than 0.5 pixels was achieved.

Relative height (rh) metrics were retrieved from the LVIS LGE product for all flight lines and measured footprints. Point data were rasterized and interpolated to 30 m Landsat base images using a Delaunay triangulation method embedded in L3Harris's ENVI software package (Boulder, CO, USA) (e.g., Sun et al, 2011; Huang et al., 2013). Four images were therefore created, corresponding to rh25, rh50, rh75 and rh100, respectively.

3.2. Selection of training and validation samples

Digital orthoimagery produced at the 0.3 m and 0.6 m resolution from aerial photos acquired between 2008 and 2011 was used to extract reference data for both training and validation purposes. The sampling unit was set to be 30 m by 30 m, consistent with the pixel size of the processed Landsat, PALSAR and LVIS data. A total of 1400 pixels were manually digitized to constitute the training sample set, including 200 pixels from each of the seven land cover classes examined in this study (Table 3). Because training data need to be representative of the classes in the classification scheme, pure pixels were intentionally selected so that the unique spectral signature of each class can be captured. The only exception was the developed class, where some sample pixels fell within residential areas and contained a mixture of vegetation (e.g. trees) and constructed materials (e.g. houses).

A probability sampling design, namely stratified random sampling, was employed to determine the location of validation samples. Preliminary analysis of an intermediate classification showed that a certain amount of pixels were erroneously labelled as evergreen, shrubland, or barren. Therefore, larger sample sizes were allocated to these three strata to ensure that each reference (or ground) class would have sufficient sample pixels to yield precise estimates of class-specific accuracy. More specifically, a simple random sample of 300 pixels was selected from the evergreen stratum, 200 pixels from barren and shrubland, respectively, and 100 pixels from each of the remaining four strata (i.e. water, developed, deciduous and herbaceous/planted), resulting in a total of 1100 pixels in the validation sample set. Each sample pixel was overlaid digitally on the orthoimagery. Reference class labels were then identified by photointerpretation, including not only a primary label of the dominant or most likely land cover class, but also an alternate label for those situations where a single class cannot cover the entire pixel or be assigned to the pixel with high confidence (Stehman and Czaplewski, 1998). This labeling protocol provides additional information on validation data quality for assessing its potential effect on the accuracy

Table 4
Single-sensor models developed using different images and features.

Data combination	Designation	Number of images	Number of features
TM leaf-on (7/15/09)	T_{on}	1	13
TM leaf-off (4/10/09)	T_{off}	1	13
TM bitemporal (4/10/09, 7/15/09)	T_2	2	26
TM multitemporal (4/10/09, 5/12/09, 7/15/09, 10/19/09)	T_4	4	52
PALSAR leaf-on (8/12/10)	P_{on}	1	30
PALSAR leaf-off (11/12/10)	P_{off}	1	30
PALSAR bitemporal* (8/12/10, 11/12/10)	P_2	2	62
PALSAR multitemporal* (5/12/10, 6/27/10, 8/12/10, 11/12/10)	P_4	4	132
LVIS	L_v	4	4

* Coherence metrics were included in the feature space for classifications that used multi-date PALSAR data.

Table 5
Two-sensor models developed using different images and features.

Data combination	Designation	Number of images	Number of features
TM leaf-on + PALSAR leaf-on	$T_{on}P_{on}$	2	43
TM leaf-on + PALSAR leaf-off	$T_{on}P_{off}$	2	43
TM leaf-on + PALSAR bitemporal	$T_{on}P_2$	3	75
TM leaf-on + PALSAR multitemporal	$T_{on}P_4$	5	145
TM leaf-off + PALSAR leaf-on	$T_{off}P_{on}$	2	43
TM leaf-off + PALSAR leaf-off	$T_{off}P_{off}$	2	43
TM leaf-off + PALSAR bitemporal	$T_{off}P_2$	3	75
TM leaf-off + PALSAR multitemporal	$T_{off}P_4$	5	145
TM bitemporal + PALSAR bitemporal	T_2P_2	4	88
TM bitemporal + PALSAR multitemporal	T_2P_4	6	158
TM multitemporal + PALSAR leaf-on	T_4P_{on}	5	82
TM multitemporal + PALSAR leaf-off	T_4P_{off}	5	82
TM multitemporal + PALSAR bitemporal	T_4P_2	6	114
TM multitemporal + PALSAR multitemporal	T_4P_4	8	184
TM multitemporal + LVIS	T_4L_v	8	56
PALSAR multitemporal + LVIS	P_4L_v	8	136

Table 6
Three-sensor models developed using different images and features.

Data combination	Designation	Number of images	Number of features
TM leaf-on + PALSAR leaf-on + LVIS	$T_{on}P_{on}L_v$	6	47
TM leaf-on + PALSAR leaf-off + LVIS	$T_{on}P_{off}L_v$	6	47
TM leaf-off + PALSAR leaf-on + LVIS	$T_{off}P_{on}L_v$	6	47
TM leaf-off + PALSAR leaf-off + LVIS	$T_{off}P_{off}L_v$	6	47
TM bitemporal + PALSAR bitemporal + LVIS	$T_2P_2L_v$	8	92
TM multitemporal + PALSAR multitemporal + LVIS	$T_4P_4L_v$	12	188

estimates (Stehman and Foody, 2009), thus has been applied in various studies including all previous NLCD accuracy assessments (e.g. Stehman et al., 2003; Wickham et al., 2004, 2010, 2013, 2017, 2021). Approximately 40% of the pixels in the validation sample set had an alternate class label (Table 3), and most were due to the identification of mixed land cover when referring to 0.3 m and 0.6 m resolution aerial photos for labeling pixels at the 30 m resolution.

3.3. Classification

Random forest (RF), an ensemble learning algorithm (Breiman, 2001), was employed in this study to assign each pixel to a specific land cover type. We opted to use RF classifiers instead of recently developed deep learning (DL) methods because: i) our dataset size was small which could lead to DL generalization issues, ii) RFs allow a better insight on individual feature performance, an important insight for our comparison, and iii) tree-based algorithms remain the classification choice for large scale mapping (e.g., the NLCD). In classification tasks, RF generates lots of classification trees, each trained on a bootstrapped sample of the original training data and searching across a random subset of the input features to determine a split at each node. The output is the majority vote of the classes predicted by individual unpruned trees. For a particular feature, its importance can be measured as the difference between classification accuracy of the out-of-bag (OOB) samples before and after permuting the values of that feature while leaving the rest unchanged. A higher accuracy decrease suggests higher importance of that feature. Compared to a single decision tree, RF classifiers largely reduce the overfitting problem and are more tolerant to outliers (or noise) in the training data (Briem et al., 2002; Chan and Paelinckx, 2008; Pal and Mather, 2003).

To explore the role of the features in land cover classification, multiple RF models were built using the same training sample set but different sensor and seasonality combinations. Specifically, nine models were developed based on features extracted from individual sensors (Table 4), and sixteen and six models by the combined use of two- and three-sensor features, respectively (Tables 5 and 6). Each model consisted of 500 classification trees, and one-third of the total number of input features were randomly picked at each splitting node. To prevent overfitting, the minimum number of samples in a leaf (or terminal) node was set to 5. All classifications were performed using the Statistics Toolbox in Mathwork's MATLAB software package (Natick, MA, USA). Feature importance was calculated when all of the 188 variables were involved, indicating the maximum discriminative capability of the datasets used in this study.

3.4. Accuracy assessment

The value of a thematic map derived from remotely sensed data directly relies on classification accuracy, a commonly accepted measure of the correctness of a classification (Foody, 2002). Accuracy assessment is therefore an essential step in classification tasks. Because validation data were collected following a probability sampling design, the establishment of statistically rigorous design-based inference for the accuracy estimates from a sample to the population can be guaranteed (Stehman, 2000). In this study, population was defined as pixels where all sensor data were available, and agreement was defined as a match between the map class and either the primary or alternate reference label to account for potential thematic ambiguity of the validation samples (Stehman et al. 2003; Wickham et al. 2004, 2010, 2013, 2017, 2021).

An error matrix was constructed to characterize classification accuracy and the performance of each RF model. While statistical tests are important, accuracy reporting was approached from the practical perspective, that is, examine whether the improvements are sufficiently meaningful to warrant the additional acquisition and process of fused datasets. The answer to this depends on the application, therefore error matrices are presented allowing each reader to come to their own conclusions with respect to their particular needs. To accommodate different sampling intensities among strata, each sample pixel was weighted inversely to its inclusion probability (i.e. the probability of a

Table 7
Estimated accuracy (%) of classifications derived from single-sensor models. Producer's and user's accuracies (PAc and UAc) are presented as deviations from corresponding accuracies of the T_4 scenario (top row, bold) with positives showing increases and negatives showing decreases.

Scenarios	Deciduous		Evergreen		Shrubland		Herbaceous/Planted		Water		Developed		Barren	
	PAc	UAc	PAc	UAc	PAc	UAc	PAc	UAc	PAc	UAc	PAc	UAc	PAc	UAc
T_4	**63**	**97**	**95**	**60**	**91**	**33**	**70**	**95**	**86**	**100**	**84**	**77**	**45**	**9**
T_2	–2	1	0	12	–1	1	2	–11	–6	0	–2	–1	13	5
T_{off}	–22	–8	–17	21	–5	–10	1	–8	–4	–1	–11	–3	51	1
T_{on}	–6	–3	–4	–14	–3	1	–24	–13	–16	0	–5	–3	50	4
P_4	–8	–5	–7	–22	–13	–6	2	–3	–8	–9	–32	1	48	–5
L_v	–12	–1	–10	–39	–56	13	–18	–4	–23	–48	–11	–21	2	–2
P_2	–9	–5	–6	–30	–26	–11	–8	–5	–11	–30	–37	–2	40	–6
P_{on}	–21	–13	–11	–33	–35	–15	–19	–7	–14	–34	–39	–15	–5	–7
P_{off}	–21	–10	–11	–35	–32	–13	–23	–8	–17	–33	–40	–16	42	–5

Table 8
Estimated accuracy (%) of classifications derived from two-sensor models. Producer's and user's accuracies (PAc and UAc) are presented as deviations from corresponding accuracies of the T_4L_v scenario (top row, bold) with positives showing increases and negatives showing decreases.

Scenarios	Deciduous		Evergreen		Shrubland		Herbaceous/Planted		Water		Developed		Barren	
	PAc	UAc	PAc	UAc	PAc	UAc	PAc	UAc	PAc	UAc	PAc	UAc	PAc	UAc
T_4L_v	**87**	**96**	**99**	**52**	**89**	**54**	**68**	**97**	**79**	**100**	**86**	**76**	**61**	**18**
T_4P_4	–22	1	–4	10	4	–21	6	1	7	0	–2	2	–15	–4
T_4P_2	–22	1	–3	10	2	–20	8	–3	6	0	–3	2	–16	–6
T_4P_{off}	–20	1	–5	9	2	–18	4	–2	6	0	–2	1	–16	–8
T_4P_{on}	–21	1	–4	8	2	–19	3	–4	6	0	–3	1	–15	–8
T_2P_4	–23	1	–6	21	2	–22	9	–2	3	0	–6	2	37	–8
T_2P_2	–24	0	–4	20	2	–20	9	–6	1	0	–4	2	–16	–9
$T_{off}P_4$	–32	0	–21	35	0	–28	10	–5	3	–1	–10	9	35	–13
$T_{on}P_4$	–28	0	–8	–3	1	–22	–2	3	–9	0	–5	1	–13	–7
$T_{off}P_2$	–36	–1	–19	37	–2	–30	10	–6	3	–1	–5	8	37	–7
$T_{on}P_2$	–30	–1	–9	–4	1	–24	–11	1	–5	0	–7	–5	–13	–10
$T_{on}P_{off}$	–30	0	–8	–6	1	–23	–13	0	–10	0	–6	–3	38	0
$T_{on}P_{on}$	–29	1	–8	–6	1	–24	–10	–2	–11	0	–8	–6	–13	–9
$T_{off}P_{off}$	–38	0	–20	29	–1	–29	–1	–7	3	–1	–7	–3	37	–9
$T_{off}P_{on}$	–44	–4	–19	36	–5	–32	7	–7	3	–1	–10	2	37	–8
P_4L_v	–35	3	–6	–30	–43	–7	–2	–3	–10	0	–13	–12	30	–14

Table 9
Estimated accuracy (%) of classifications derived from three-sensor models. Producer's and user's accuracies (PAc and UAc) are presented as deviations from corresponding accuracies of the $T_4P_4L_v$ scenario (top row, bold) with positives showing increases and negatives showing decreases.

Scenarios	Deciduous		Evergreen		Shrubland		Herbaceous/Planted		Water		Developed		Barren	
	PAc	UAc	PAc	UAc	PAc	UAc	PAc	UAc	PAc	UAc	PAc	UAc	PAc	UAc
$T_4P_4L_v$	**87**	**96**	**99**	**54**	**91**	**61**	**72**	**99**	**88**	**100**	**87**	**77**	**48**	**14**
$T_2P_2L_v$	–1	1	–1	5	0	–4	–5	–1	–5	0	0	–1	52	–5
$T_{off}P_{on}L_v$	–5	2	–5	5	–31	9	–1	–5	–5	–1	–9	–17	50	–1
$T_{off}P_{off}L_v$	–5	2	–4	7	–32	10	–4	–6	–6	–1	–9	–16	50	–4
$T_{on}P_{on}L_v$	–5	2	–5	–20	–9	–7	–11	–4	–18	0	–6	–3	51	6
$T_{on}P_{off}L_v$	–4	2	–4	–22	–20	–4	–14	–5	–18	0	–8	–4	50	2

particular pixel being included in the sample set). Because the seven strata used for validation sample selection are based on an intermediate classification map and do not exactly correspond to any classification scenario examined, cell proportions of the error matrix and the accompanying accuracy measures, including overall accuracy and class-specific user's and producer's accuracies, were estimated following the formulas presented in Stehman (2014). Standard errors of the accuracy estimates were also computed, quantifying the degree of uncertainty due to sampling variation of validation data. Accuracy results were reported for each classified map with different features as classification inputs.

4. Results and discussion

4.1. Accuracy of classifications derived from different data inputs

4.1.1. Impact of multi-date fusion on classification accuracy

Tables 7–9 summarize accuracies of the single-, two-, and three-sensor classifications with designated names presented in Tables 4–6, respectively. For each table, results are listed in descending order of overall accuracy (reported in Fig. 5), and user's accuracy (UAc) and producer's accuracy (PAc) are presented as deviations from corresponding accuracies of the scenario that has the highest overall accuracy to facilitate a more straightforward assessment of the differences among classifications. All accuracy estimates are rounded to the nearest whole number. Standard errors of the overall accuracy are around 2% in all classification scenarios.

Overall accuracies of single-sensor classifications ranged from 48% to 74% (Fig. 5). Among all single-sensor scenarios, the highest overall accuracy was achieved through the integration of multitemporal Landsat data (T_4), and was about 1% higher than the overall accuracy of the two-date Landsat classification (T_2) and 10% higher than the single-date Landsat overall accuracies (T_{on} or T_{off}). Similarly, compared to the single- and two-date PALSAR classifications, combining multitemporal PALSAR data improved overall accuracies by 14–15% and 8–9%,

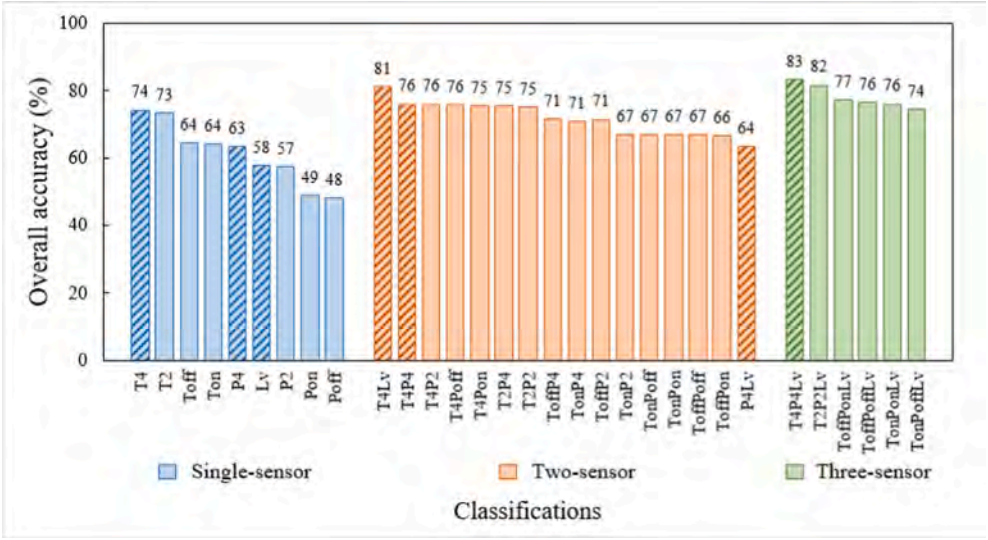

Fig. 5. Overall accuracy of all classifications performed in this study. A descending order is applied to the single-, two- and three-sensor scenarios, respectively. Columns filled with upward diagonals correspond to the scenarios presented in Table 10.

Table 10
Estimated accuracy (%) of classifications developed using combinations of different sensor data. Producer's and user's accuracies (PAc and UAc) are presented as deviations from corresponding accuracies of the $T_4P_4L_v$ scenario (top row, bold) with positives showing increases and negatives showing decreases.

Scenarios	Deciduous		Evergreen		Shrubland		Herbaceous/Planted		Water		Developed		Barren	
	PAc	UAc	PAc	UAc	PAc	UAc	PAc	UAc	PAc	UAc	PAc	UAc	PAc	UAc
$T_4P_4L_v$	**87**	**96**	**99**	**54**	**91**	**61**	**72**	**99**	**88**	**100**	**87**	**77**	**48**	**14**
T_4L_v	0	0	0	–2	–2	–7	–4	–2	–8	0	–2	0	13	4
T_4P_4	–23	1	–4	8	2	–28	2	–1	–1	0	–4	1	–3	1
T_4	–25	1	–4	6	1	–28	–2	–3	–2	0	–4	0	–3	–5
P_4L_v	–35	3	–6	–32	–45	–14	–6	–5	–18	0	–15	–13	43	–9
P_4	–32	–4	–11	–15	–12	–34	0	–6	–10	–9	–35	1	45	–10
L_v	–37	0	–14	–33	–55	–15	–20	–8	–25	–48	–14	–20	–1	–7

respectively. The choice of sensor also had considerable impact on overall accuracy. Classifications of Landsat data resulted in overall accuracies of 64–74%, consistently higher than overall accuracies of PALSAR (48–63%) and LVIS (58%) classifications. More substantial differences in accuracy were associated with certain classes (Table 7). For example, producer's accuracies of shrubland and developed and user's accuracies of evergreen and water varied by 40–56% with regard to the use of different sensor data.

Moving to the two-sensor classifications (Fig. 5, Table 8), a 17% difference in overall accuracy was observed among the numerous combinations. Starting with the lowest performer, multi-date PALSAR combined with LVIS data (P_4L_v) was able to classify different land cover types to 64%, an overall accuracy inferior to all other two-sensor scenarios. Using single-date Landsat and PALSAR data resulted in classifications with a nearly identical overall accuracy of 67%. Including all PALSAR observations increased overall accuracy to 71% ($T_{off}P_4$ and $T_{on}P_4$), which was further improved to 76% by incorporating multi-date Landsat observations also (T_4P_4). The most accurate two-sensor classification was generated with the joint use of LVIS and multitemporal Landsat data as classification inputs (T_4L_v), and an overall accuracy of 81% was achieved. Compared to T_4P_4, substantial improvement was associated with the deciduous and shrubland classes, as producer's accuracy of deciduous and user's accuracy of shrubland were increased by more than 20%. It should be noted that although the exclusive use of PALSAR (P_4) led to a 5% higher overall accuracy than was obtained by using LVIS alone (L_v) (63% vs. 58%, Table 7), greater improvement was gained when combining multitemporal Landsat images with LVIS data as opposed to PALSAR, suggesting that LVIS contributed more useful thematic information that are complementary to Landsat data and beneficial to the classification task.

Performance of three-sensor classifications was relatively close compared to that of single- and two-sensor scenarios with overall accuracy varying from 74% to 83% (Fig. 5, Table 9). Similar overall accuracies of 74–77% were attained with the fusion of single-date Landsat, PALSAR and LVIS data. Nonetheless, replacing the leaf-on with the leaf-off Landsat scene gave rise to a nearly 30% increase in user's accuracy of evergreen and a 10% increase in producer's accuracy of herbaceous/planted ($T_{on}P_{off}L_v$ vs. $T_{off}P_{off}L_v$, $T_{on}P_{on}L_v$ vs. $T_{off}P_{on}L_v$). The integration of Landsat and PALSAR leaf-on and leaf-off pairs with LVIS data increased overall accuracy to 82% ($T_2P_2L_v$). Another 1% improvement was achieved by the further addition of Landsat and PALSAR images acquired during the transitional period ($T_4P_4L_v$), leading to the highest overall accuracy of 83%. Specifically, producer's accuracies of shrubland and developed were considerably improved to 91% and 87% when fusing two- or multi-date Landsat and PALSAR with LVIS data, whereas user's accuracies of deciduous and water were consistently higher than 96% for all three-sensor scenarios.

To examine the impact of including alternate labels for validation, accuracies of all classification scenarios were also calculated following a more strict agreement defined as a match between the map class and the primary label only (see Appendix A). Overall accuracies reported in Fig. A.1 are 6–9% lower compared to those present in Fig. 5. This is consistent with the general expectation considering the fact that the existence of mixed pixels was ignored and no allowance was permitted for any thematic ambiguity in the reference class labels. However, the relative performance of the different combinations of sensor types and dates remains fundamentally the same, although the absolute values of increase or decrease may be different (Table A.1).

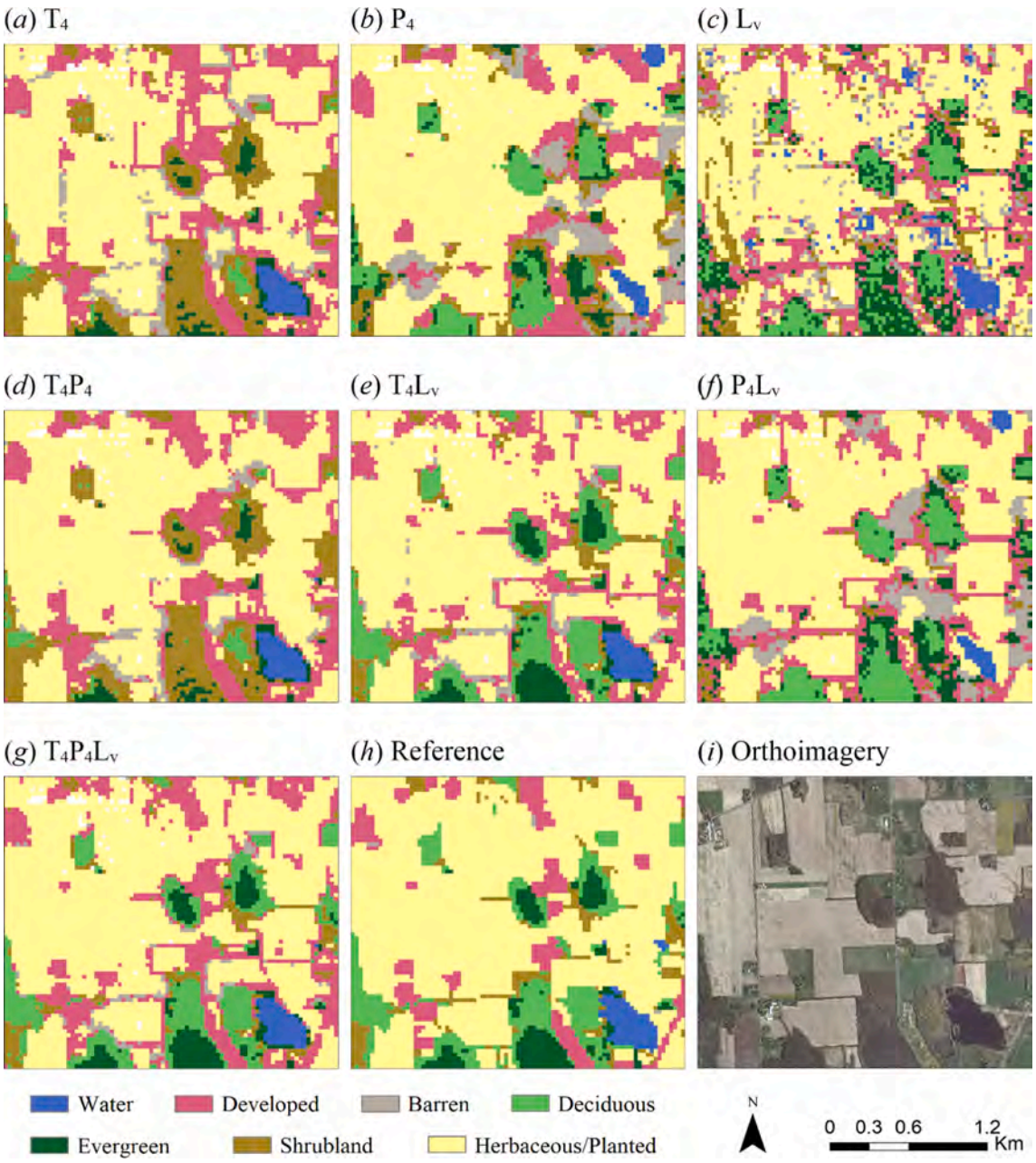

Fig. 6. Land cover maps created using different sensor combinations (*a*)-(*g*), and by manually assigning each 30 m pixel a reference class (*h*) based on the 0.6 m resolution orthoimagery (*i*). Pixels containing no LVIS LiDAR footprints (displayed in white, (*a*)-(*g*)) were excluded from classification and accuracy assessment.

Table 11
Error matrix and associated accuracy estimates (%) of the classification using multitemporal Landsat and PALSAR data as inputs (T_4P_4). Overall accuracy is 76% with a standard error (SE) of 2%.

Class	Water	Developed	Barren	Deciduous	Evergreen	Shrubland	Herbaceous/Planted	Total	UAc (SE)
Water	**3.734**	0.000	0.000	0.000	0.000	0.000	0.000	3.734	100 (0)
Developed	0.053	**21.361**	0.372	1.292	0.000	0.036	4.249	27.363	78 (4)
Barren	0.000	1.064	**0.308**	0.000	0.000	0.002	0.778	2.153	14 (5)
Deciduous	0.043	0.311	0.000	**19.362**	0.100	0.201	0.036	20.052	97 (1)
Evergreen	0.387	0.418	0.000	0.998	**3.230**	0.093	0.107	5.234	62 (7)
Shrubland	0.107	2.381	0.000	8.002	0.057	**6.374**	2.431	19.353	33 (4)
Herbaceous/Planted	0.000	0.036	0.000	0.275	0.000	0.179	**21.622**	22.111	98 (1)
Total	4.324	25.572	0.680	29.929	3.387	6.884	29.224	100	
PAc (SE)	86 (3)	84 (4)	45 (22)	65 (4)	95 (2)	93 (2)	11 4)		

Table 12
Error matrix and associated accuracy estimates (%) of the classification combining LVIS with multitemporal Landsat and PALSAR data as inputs ($T_4P_4L_v$). Overall accuracy is 83% with a standard error (SE) of 2%.

Class	Water	Developed	Barren	Deciduous	Evergreen	Shrubland	Herbaceous/Planted	Total	UAc (SE)
Water	**3.734**	0.000	0.000	0.000	0.000	0.000	0.000	3.734	100 (0)
Developed	0.021	**21.810**	0.336	1.292	0.000	0.036	4.985	28.481	77 (4)
Barren	0.000	1.064	**0.308**	0.332	0.000	0.002	0.556	2.263	14 (5)
Deciduous	0.021	0.729	0.000	**27.768**	0.000	0.468	0.021	29.007	96 (2)
Evergreen	0.468	0.693	0.000	1.579	**3.406**	0.043	0.107	6.297	54 (6)
Shrubland	0.021	0.439	0.000	0.826	0.036	**5.645**	2.345	9.313	61 (6)
Herbaceous/Planted	0.000	0.222	0.000	0.000	0.000	0.036	**20.648**	20.906	99 (1)
Total	4.266	24.958	0.644	31.797	3.442	6.230	28.663	100	
PAc (SE)	88 (3)	87 (4)	48 (25)	87 (2)	99 (1)	91 (5)	72 (4)		

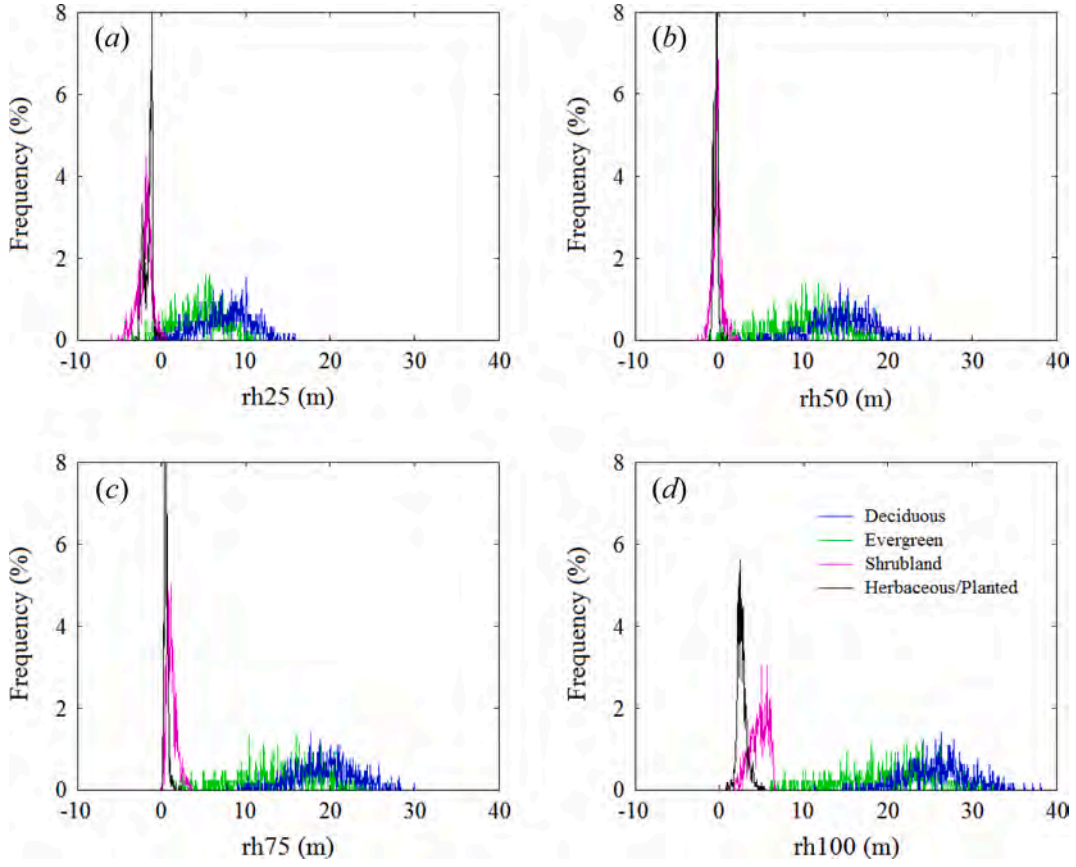

Fig. 7. Histograms of the four vegetation types in the LVIS-derived height metrics: (*a*) rh25, (*b*) rh50, (*c*) rh75, and (*d*) rh100.

4.1.2. Impact of multi-sensor fusion on classification accuracy

Accuracies derived from combinations of different types of features associated with one, two or three sensors were summarized in Table 10 (also see the columns filled with upward diagonals in Fig. 5). Fusing LVIS with multitemporal PALSAR data (P_4L_v) increased overall accuracy by 6% and 1%, compared to the use of each dataset individually. The integration of Landsat with PALSAR (T_4P_4) and Landsat with LVIS (T_4L_v) contributed to more substantial improvement in classification performance over single-sensor classifications. For example, an increase of 13% and 23% in overall accuracy was respectively attained due to the addition of Landsat data relative to using PALSAR or LVIS alone (T_4P_4 vs. P_4, T_4L_v vs. L_v). As expected, combining the features derived from all three sensors led to the highest overall accuracy of 83% ($T_4P_4L_v$), 2–19% superior to the two-sensor scenarios. The slight improvement of 2% over T_4L_v implies that the benefits of introducing SAR features to Landsat and LVIS were limited for classifying the land cover types present at the study site. It should be noted that when Landsat data were available, the inclusion of LVIS data was capable of improving overall accuracy by 7% (T_4L_v vs. T_4, $T_4P_4L_v$ vs. T_4P_4), a larger extent over the 1% improvement obtained by adding LVIS to PALSAR only (P_4L_v vs. P_4). This indicates that LVIS-derived height metrics can be more successful in discriminating different land cover types with the combined use of Landsat data. Differences in class-specific accuracies were more noticeable for certain vegetation-related classes like deciduous, evergreen and shrubland, as well as the developed class that was defined as a mixture of constructed materials (i.e. impervious surface) and vegetation planted for recreation, erosion control and aesthetic purposes.

The corresponding classified maps were also evaluated qualitatively. Although an intensive inspection at multiple locations was conducted, classifications over a small area consisting of 85 by 75 30-m pixels were presented in Fig. 6 to facilitate a clearer interpretation. A reference land cover classification, as Fig. 6h shows, was generated by visually identifying the dominant class of every 30 m pixel based on the orthoimagery at the 0.6 m resolution over the selected area (Fig. 6i). Substantial differences can be observed when comparing Fig. 6g, the resultant map of $T_4P_4L_v$ classification, to the other six maps derived from single- and two-

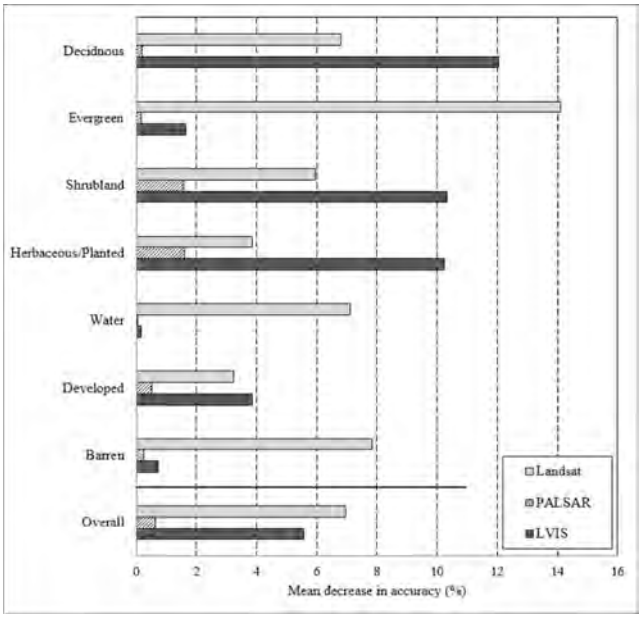

Fig. 8. Averaged feature importance for each land cover class and over all classes.

sensor classifications (Fig. 6a-f), and Fig. 6g appears more consistent with the real land cover patterns as displayed in Fig. 6h and i. Specifically, in Fig. 6g, the confusion between deciduous and shrubland in Fig. 6a and d was considerably reduced, and only a small number of pixels were classified as barren, as opposed to Fig. 6b and f, where large barren patches were erroneously created. Besides, lower spatial heterogeneity was achieved in Fig. 6g compared to Fig. 6c and e, and artifacts and isolated pixels that are most likely to be noise were largely removed. Despite the overall consistency, the comparison of Fig. 6g and h also reveals that certain misclassification occurred between the herbaceous/planted and developed classes. This may be largely due to the difficulties in separating natural and semi-natural herbaceous and planted areas (e.g. croplands) from grass-covered ground in the developed context (e.g. residential backyards and golf courses). Nonetheless, this assessment still proved that the model developed using Landsat, PALSAR and LVIS data concurrently can generate a visually more reliable land cover classification over multiple land cover types with varying extents of ground coverage.

4.2. Added value of LiDAR observations in characterizing vegetation

To further evaluate the contribution of LVIS in improving class-specific accuracies, a comparison was conducted between the two classifications before and after LVIS data were fused with multitemporal Landsat and PALSAR images as inputs (T_4P_4 vs. $T_4P_4L_v$). Tables 11 and 12 show the error matrix of the two classified maps created over the entire study area, respectively. The rows represent remote sensing-derived classification and the columns correspond to ground reference. Cell entries are expressed as proportion of area. The diagonal cells summarize correctly classified areas (displayed in bold), and all off-diagonal cells indicate errors.

Disagreement was largely associated with the deciduous and shrubland classes in the T_4P_4 classification, as displayed in a light gray color in Table 11. Substantial deciduous pixels were misclassified as shrubland, resulting in remarkably high omission error of deciduous and high commission error of shrubland. This is mainly attributed to the similarities of the two vegetation classes in their spectral, scattering and temporal signatures. In contrast, vertical structural features extracted from LiDAR waveforms played a crucial role in distinguishing shrubland from deciduous forest. As shown in Table 12, including LVIS relative height (rh) metrics largely resolved the problem, and predominantly contributed to the 28% increase in user's accuracy of shrubland and the 23% increase in producer's accuracy of deciduous. Specifically, signatures of the deciduous, evergreen, shrubland, and herbaceous/planted classes were explored with respect to each rh metric based on the reference data (Fig. 7). It is clear to see that the separability of shrubland and deciduous was high, especially in rh75 and rh100. Also, Fig. 7d coincides with the commonly adopted definition of shrubland as areas of shrubs and young trees less than 5 m tall, whereas deciduous/evergreen forest referring to areas dominated by trees that are generally greater than 5 m tall. The fact that deciduous overlaps with evergreen to a large degree in all of the four rh metrics caused the two classes hard to separate, a major limitation of using LVIS alone. This could largely be compensated by the integration of multitemporal Landsat data due to additional information on seasonal changes they brought in (Table 10).

Among the seven land cover types, barren was always the least well characterized with the lowest producers' and user's accuracies. According to Tables 11 and 12, omission error of the barren class is attributed to the fact that more than 50% of barren pixels were labeled as developed. Meanwhile, the majority of pixels classified as barren were actually developed or herbaceous/planted on the ground, giving rise to its markedly high commission error. Nonetheless, its impact on the overall quality of the resultant classified maps is considered marginal, since barren is a rare class that represents only 2% of the study area from the map perspective.

4.3. Importance of sensor type to individual classes

To examine the relevant importance of spectral, scattering and vertical structural features in land cover classification, an assessment was implemented on the classifier that combined all of the 188 variables extracted from Landsat, PALSAR and LVIS data as classification inputs (T_4P_4Lv). The variables were grouped into three feature sets, each corresponding to a specific sensor and sensor type. Importance was measured as the mean decrease in accuracy as a result of the OOB samples being misclassified providing that the four most important features in the feature set evaluated was absent (Fig. 8, also see Fig. B.1 and Table B.1 in Appendix B for the importance of individual features).

Compared to PALSAR and LVIS, the Landsat feature set was of greater importance to the overall accuracy. Both Landsat and LVIS contributed considerably more than the numerous PALSAR-derived features, since randomly permuting values of those features yielded a slightly decreased overall accuracy by less than 1%. LVIS was the most indispensable feature set for three out of the four vegetation classes assessed in this study: deciduous, shrubland and herbaceous/planted. The critical role that multitemporal Landsat data played in mapping evergreen, as discussed in Section 4.2, was confirmed by the fact that when Landsat features were removed, the chance an evergreen pixel

labeled as any other class increased by 14%. The integration of the PALSAR feature set was more beneficial to shrubland and herbaceous/planted over the other classes.

5. Conclusions

This study illustrates that integration of spaceborne optical (Landsat-5/TM) and SAR (ALOS-1/PALSAR) and airborne full-waveform LiDAR (LVIS) data provides the most pronounced discriminative power among different land cover types. An overall accuracy of 83% was achieved when all spectral, scattering and vertical structural features were used as classification inputs, 2–19% and 9–25% higher than the numerous two-sensor and single-sensor scenarios assessed, respectively. The inclusion of seasonal spectral and scattering variations of vegetation classes also improved overall accuracy by nearly 10%, when observations from all three sensors were used in combination. Compared to PALSAR features, LVIS-derived canopy height metrics contributed more useful thematic information that is complementary to Landsat data and beneficial to classification performance, especially for vegetation classes. As more applications and studies of spaceborne GEDI LiDAR emerge, this study serves as a guide regarding to what extent accuracy of classification maps may be improved through the fusion of multi-date and multi-type remotely sensed data with a commonly used classifier of random forest. Future work will be focused on extending our current proof-of-concept work to additional sites, sensors and time periods with the use of other machine learning as well as advanced deep learning algorithms that have gained a lot of interest recently to ensure more generalized and statistically representative conclusions.

Declaration of Competing Interest

The authors declare that they have no known competing financial interests or personal relationships that could have appeared to influence the work reported in this paper.

Acknowledgements

This work was partially supported through NSF's Macrosystems Biology and NEON-Enabled Science (MSB-NES) Program to H. Jin [grant number 2106030] and NASA's Biodiversity Program to G. Mountrakis [grant number NNX09AK16G]. We sincerely thank the four anonymous reviewers and the associate editor for their careful review and many constructive comments and suggestions that helped improve the manuscript.

Appendix A

See Table A1 and Fig. A1.

Table A1
Producer's and user's accuracies (%) of classifications derived from single-, two- and three-sensor models, where agreement is defined as a match between the map class and the primary reference label only for the validation samples. The table is formatted to be consistent with Tables 7–9 in the text.

Scenarios	Deciduous		Evergreen		Shrubland		Herbaceous/Planted		Water		Developed		Barren	
	PAc	UAc	PAc	UAc	PAc	UAc	PAc	UAc	PAc	UAc	PAc	UAc	PAc	UAc
(*a*) *Single-sensor classifications*														
T_4	**57**	**91**	**66**	**44**	**80**	**23**	**65**	**93**	**85**	**100**	**81**	**68**	**45**	**9**
T_2	0	1	4	6	−1	2	2	−11	−6	0	−3	1	−1	−1
T_{off}	−21	−8	−3	8	−10	−8	3	−8	−6	−10	−13	−1	−3	−3
T_{on}	−8	−5	−7	−20	−4	−5	−24	−14	−18	0	−8	−2	49	1
P_4	−10	−12	−11	−25	−28	−10	0	−5	−13	−17	−33	3	2	−5
L_v	−14	−4	−12	−33	−57	1	−16	−8	−25	−49	−14	−18	−28	−7
P_2	−10	−7	−6	−25	−40	−12	−8	−8	−16	−37	−38	−1	−3	−6
P_{on}	−20	−16	−12	−27	−45	−14	−18	−11	−15	−34	−41	−14	−6	−7
P_{off}	−21	−16	−18	−31	−42	−13	−23	−11	−21	−41	−41	−13	−8	−7
(*b*) *Two-sensor classifications*														
T_4L_v	**87**	**96**	**99**	**52**	**89**	**54**	**68**	**97**	**79**	**100**	**86**	**76**	**61**	**18**
T_4P_4	−30	−5	−34	−7	−9	−31	1	−2	6	0	−6	−6	−16	−4
T_4P_2	−29	−5	−33	−7	−11	−30	2	−5	6	0	−6	−6	−16	−6
T_4P_{off}	−27	−5	−36	−8	−9	−28	−2	−5	6	0	−5	−8	−16	−8
T_4P_{on}	−27	−5	−34	−5	−10	−29	−2	−6	6	0	−6	−8	−16	−8
T_2P_4	−23	1	−6	21	2	−22	9	−2	3	0	−6	2	37	−8
T_2P_2	−29	−6	−31	−1	−11	−29	3	−8	0	0	−8	−5	−16	−9
$T_{off}P_4$	−32	0	−21	35	0	−28	10	−5	3	−1	−10	9	35	−13
$T_{off}P_2$	−36	−1	−19	37	−2	−30	10	−6	3	−1	−5	8	37	−7
$T_{on}P_4$	−36	−7	−40	−24	−11	−35	−9	−1	−11	0	−10	−8	−16	−7
$T_{off}P_{off}$	−42	−6	−35	0	−16	−36	−6	−9	0	−10	−12	−8	−18	−13
$T_{off}P_{on}$	−48	−13	−33	6	−20	−39	2	−9	0	−10	−15	−3	−18	−12
$T_{on}P_2$	−30	−1	−9	−4	1	−24	−11	1	−5	0	−7	−5	−13	−10
$T_{on}P_{off}$	−38	−8	−40	−25	−10	−35	−19	−2	−12	0	−12	−12	32	−5
$T_{on}P_{on}$	−38	−6	−39	−26	−15	−35	−17	−8	−12	0	−13	−15	−16	−9
P_4L_v	−35	3	−6	−30	−43	−7	−2	−3	−10	0	−13	−12	30	−14
(*c*) *Three-sensor classifications*														
$T_4P_4L_v$	**87**	**96**	**99**	**54**	**91**	**61**	**72**	**99**	**88**	**100**	**87**	**77**	**48**	**14**
$T_2P_2L_v$	−1	1	−1	5	0	−4	−5	−1	−5	0	0	−1	52	−5
$T_{off}P_{on}L_v$	−5	2	−5	5	−31	9	−1	−5	−5	−1	−9	−17	50	−1
$T_{off}P_{off}L_v$	−5	2	−4	7	−32	10	−4	−6	−6	−1	−9	−16	50	−4
$T_{on}P_{on}L_v$	−5	2	−5	−20	−9	−7	−11	−4	−18	0	−6	−3	51	6
$T_{on}P_{off}L_v$	−4	2	−4	−22	−20	−4	−14	−5	−18	0	−8	−4	50	2

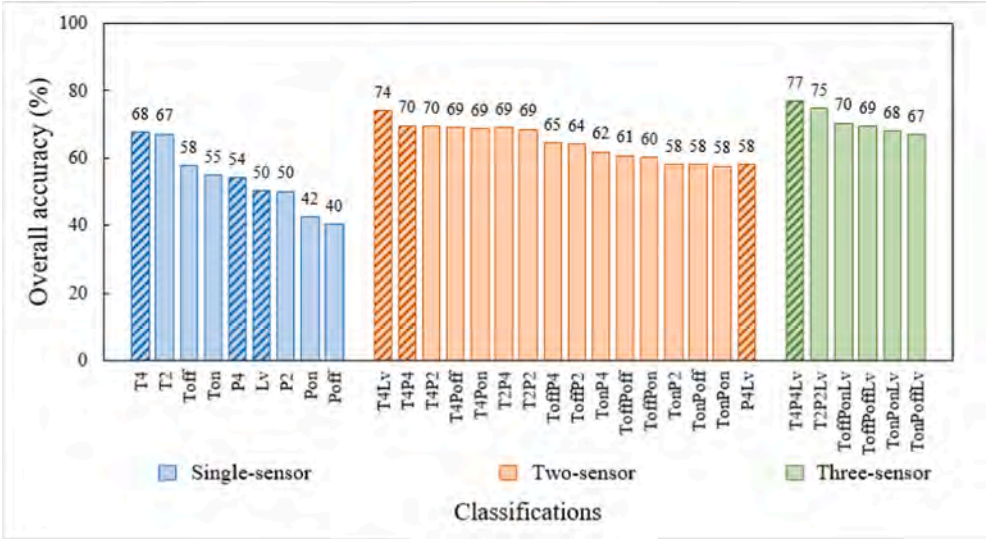

Fig. A1. Overall accuracy of single-, two- and three-sensor classifications, where agreement is defined as a match between the map class and the primary reference label only for the validation samples. The figure is formatted to be consistent with Fig. 5 in the text.

Appendix B

See Fig. B1 and Table B1.

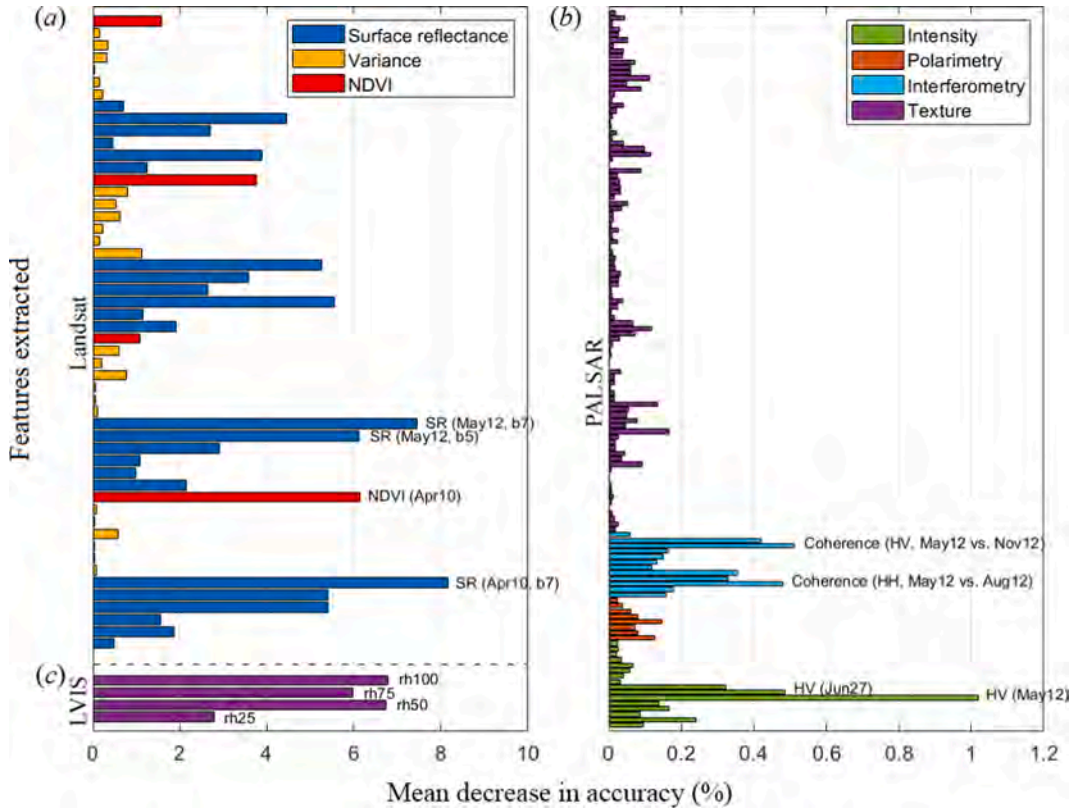

Fig. B1. Importance of all features extracted from (*a*) Landsat, (*b*) PALSAR, and (*c*) LVIS data. Note that subplots (*a*) and (*c*) are combined due to the similar scale of 0–10%.

Table B1
Importance of all Landsat, PALSAR, and LVIS features used for classification (expressed in percent). Shading is applied to the four most important features of each dataset that are labeled in Fig. B.1.

(*a*) Landsat (52)				(*b*) PALSAR* (132)											
4/10		7/15		Intensity		Interferometry (γ)		Texture (8/12, w3)		Texture (5/12, w3)		Texture (6/27, w3)		Texture (11/12, w3)	
SR (b1)	0.49	SR (b1)	1.91	HH (8/12)	0.10	γ_{HH}	0.16	HOM_{HH}	0.02	HOM_{HH}	0.01	HOM_{HH}	0.02	HOM_{HH}	0.01
SR (b2)	1.85	SR (b2)	1.16	HH (5/12)	0.24	(8/12 vs. 11/12)		CON_{HH}	0.03	CON_{HH}	0.02	CON_{HH}	0.02	CON_{HH}	0.02
SR (b3)	1.56	SR (b3)	5.54	HH (6/27)	0.09	γ_{HH}	0.18	DIS_{HH}	0.02	DIS_{HH}	0.01	DIS_{HH}	0.02	DIS_{HH}	0.01
SR (b4)	5.41	SR (b4)	2.65	HH (11/12)	0.17	(6/27 vs. 8/12)		ENT_{HH}	0.01	ENT_{HH}	0.02	ENT_{HH}	0.01	ENT_{HH}	0.00
SR (b5)	5.40	SR (b5)	3.56	HV (8/12)	0.14	γ_{HH}	0.48	ENE_{HH}	0.00	ENE_{HH}	0.01	ENE_{HH}	0.00	ENE_{HH}	0.01
SR (b7)	8.16	SR (b7)	5.27	HV (5/12)	1.02	(5/12 vs. 8/12)		COR_{HH}	0.01	COR_{HH}	0.03	COR_{HH}	0.02	COR_{HH}	0.02
Var (b1)	0.09	Var (b1)	1.12	HV (6/27)	0.49	γ_{HH}	0.33	HOM_{HV}	0.01	HOM_{HV}	0.00	HOM_{HV}	0.01	HOM_{HV}	0.04
Var (b2)	0.03	Var (b2)	0.15	HV (11/12)	0.32	(5/12 vs. 11/12)		CON_{HV}	0.01	CON_{HV}	0.00	CON_{HV}	0.03	CON_{HV}	0.01
Var (b3)	0.03	Var (b3)	0.22	HH–HV (8/12)	0.03	γ_{HH}	0.35	DIS_{HV}	0.01	DIS_{HV}	0.01	DIS_{HV}	0.01	DIS_{HV}	0.02
Var (b4)	0.58	Var (b4)	0.64	HH–HV (5/12)	0.04	(5/12 vs. 6/27)		ENT_{HV}	0.00	ENT_{HV}	0.00	ENT_{HV}	0.01	ENT_{HV}	0.09
Var (b5)	0.04	Var (b5)	0.53	HH–HV (6/27)	0.06	γ_{HH}	0.12	ENE_{HV}	0.00	ENE_{HV}	0.01	ENE_{HV}	0.01	ENE_{HV}	0.05
Var (b7)	0.08	Var (b7)	0.80	HH–HV (11/12)	0.07	(6/27 vs. 11/12)		COR_{HV}	0.01	COR_{HV}	0.03	COR_{HV}	0.03	COR_{HV}	0.11
NDVI	6.14	NDVI	3.77	HH/HV (8/12)	0.04	γ_{HV} (8/12 vs. 11/12)	0.13	Texture (8/12, w15)		Texture (5/12, w15)		Texture (6/27, w15)		Texture (11/12, w15)	
5/12		10/19		HH/HV (5/12)	0.02			HOM_{HH}	0.09	HOM_{HH}	0.07	HOM_{HH}	0.05	HOM_{HH}	0.06
SR (b1)	2.16	SR (b1)	1.25	HH/HV (6/27)	0.03	γ_{HV}	0.15	CON_{HH}	0.04	CON_{HH}	0.12	CON_{HH}	0.02	CON_{HH}	0.06
SR (b2)	0.98	SR (b2)	3.89	HH/HV (11/12)	0.02	(6/27 vs. 8/12)		DIS_{HH}	0.04	DIS_{HH}	0.07	DIS_{HH}	0.03	DIS_{HH}	0.07
SR (b3)	1.07	SR (b3)	0.46	Polarimetry (H, α)		γ_{HV}	0.17	ENT_{HH}	0.02	ENT_{HH}	0.01	ENT_{HH}	0.03	ENT_{HH}	0.04
SR (b4)	2.90	SR (b4)	2.70	α (8/12)	0.13	(5/12 vs. 8/12)		ENE_{HH}	0.02	ENE_{HH}	0.01	ENE_{HH}	0.03	ENE_{HH}	0.04
SR (b5)	6.11	SR (b5)	4.46	H (8/12)	0.08	γ_{HV}	0.51	COR_{HH}	0.03	COR_{HH}	0.03	COR_{HH}	0.02	COR_{HH}	0.01
SR (b7)	7.44	SR (b7)	0.70	α (5/12)	0.07	(5/12 vs. 11/12)		HOM_{HV}	0.17	HOM_{HV}	0.04	HOM_{HV}	0.09	HOM_{HV}	0.05
Var (b1)	0.11	Var (b1)	0.23	H (5/12)	0.15	γ_{HV}	0.42	CON_{HV}	0.05	CON_{HV}	0.01	CON_{HV}	0.00	CON_{HV}	0.03
Var (b2)	0.07	Var (b2)	0.15	α (6/27)	0.08	(5/12 vs. 6/27)		DIS_{HV}	0.08	DIS_{HV}	0.01	DIS_{HV}	0.01	DIS_{HV}	0.03
Var (b3)	0.05	Var (b3)	0.04	H (6/27)	0.06	γ_{HV}	0.06	ENT_{HV}	0.05	ENT_{HV}	0.03	ENT_{HV}	0.11	ENT_{HV}	0.01
Var (b4)	0.78	Var (b4)	0.33	α (11/12)	0.04	(6/27 vs. 11/12)		ENE_{HV}	0.06	ENE_{HV}	0.03	ENE_{HV}	0.10	ENE_{HV}	0.04
Var (b5)	0.20	Var (b5)	0.34	H (11/12)	0.02			COR_{HV}	0.14	COR_{HV}	0.03	COR_{HV}	0.04	COR_{HV}	0.02
Var (b7)	0.60	Var (b7)	0.15												
NDVI	1.08	NDVI	1.58												
(*c*) LVIS (4)															
rh25	2.80	rh50	6.72	rh75	5.96	rh100	6.79								

* For a full description of the numerous PALSAR features and how they are calculated the reader is referred to Jin et al. (2014).

References

Adams, B.T., Matthews, S.N., 2018. Enhancing forest and shrubland mapping in a managed forest landscape with Landsat–LiDAR data fusion. Nat. Areas J. 38 (5), 402–418.

Adrian, J., Sagan, V., Maimaitijiang, M., 2021. Sentinel SAR-optical fusion for crop type mapping using deep learning and Google Earth Engine. ISPRS J. Photogramm. Remote Sens. 175, 215–235.

Adriano, B., Xia, J., Baier, G., Yokoya, N., Koshimura, S., 2019. Multi-source data fusion based on ensemble learning for rapid building damage mapping during the 2018 Sulawesi earthquake and tsunami in Palu, Indonesia. *Remote Sens.* 11 (7), 886.

Alonzo, M., Bookhagen, B., Roberts, D.A., 2014. Urban tree species mapping using hyperspectral and lidar data fusion. Remote Sens. Environ. 148, 70–83.

Amarsaikhan, D., Blotevogel, H.H., van Genderen, J.L., Ganzorig, M., Gantuya, R., Nergui, B., 2010. Fusing high-resolution SAR and optical imagery for improved urban land cover study and classification. Int. J. Image Data Fusion 1 (1), 83–97.

Attarchi, S., Gloaguen, R., 2014. Classifying complex mountainous forests with L-Band SAR and Landsat data integration: A comparison among different machine learning methods in the Hyrcanian Forest. Remote Sens. 6 (5), 3624–3647.

Blaes, X., Vanhalle, L., Defourny, P., 2005. Efficiency of crop identification based on optical and SAR image time series. Remote Sens. Environ. 96 (3-4), 352–365.

Blair, J.B., Hofton, M.A., Rabine, D.L., 2006. Processing of NASA LVIS elevation and canopy (LGE, LCE and LGW) data products, version 1.02. <http://lvis.gsfc.nasa.gov>.

Blair, J.B., Rabine, D.L., Hofton, M.A., 1999. The Laser Vegetation Imaging Sensor: A medium-altitude, digitisation-only, airborne laser altimeter for mapping vegetation and topography. ISPRS J. Photogramm. Remote Sens. 54 (2-3), 115–122.

Bork, E.W., Su, J.G., 2007. Integrating LIDAR data and multispectral imagery for enhanced classification of rangeland vegetation: A meta analysis. Remote Sens. Environ. 111 (1), 11–24.

Breiman, L., 2001. Random forests. Machine Learn. 45, 5–32.

Briem, G.J., Benediktsson, J.A., Sveinsson, J.R., 2002. Multiple classifiers applied to multisource remote sensing data. IEEE Trans. Geosci. Remote Sens. 40 (10), 2291–2299.

Cai, Y., Li, X., Zhang, M., Lin, H., 2020. Mapping wetland using the object-based stacked generalization method based on multi-temporal optical and SAR data. Int. J. Appl. Earth Obs. Geoinf. 92, 102164. https://doi.org/10.1016/j.jag.2020.102164.

Chan, J.-W., Paelinckx, D., 2008. Evaluation of Random Forest and Adaboost tree-based ensemble classification and spectral band selection for ecotope mapping using airborne hyperspectral imagery. Remote Sens. Environ. 112 (6), 2999–3011.

Chapin III, F.S., Zavaleta, E.S., Eviner, V.T., Naylor, R.L., Vitousek, P.M., Reynolds, H.L., Hooper, D.U., Lavorel, S., Sala, O.E., Hobbie, S.E., Mack, M.C., Díaz, S., 2000. Consequences of changing biodiversity. Nature 405 (6783), 234–242.

Cho, M.A., Mathieu, R., Asner, G.P., Naidoo, L., van Aardt, J., Ramoelo, A., Debba, P., Wessels, K., Main, R., Smit, I.P.J., Erasmus, B., 2012. Mapping tree species composition in South African savannas using an integrated airborne spectral and LiDAR system. Remote Sens. Environ. 125, 214–226.

Chust, G., Ducrot, D., Pretus, J.LL., 2004. Land cover discrimination potential of radar multitemporal series and optical multispectral images in a Mediterranean cultural landscape. Int. J. Remote Sens. 25 (17), 3513–3528.

Cihlar, J., 2000. Land cover mapping of large areas from satellites: Status and research priorities. Int. J. Remote Sens. 21 (6-7), 1093–1114.

Dalponte, M., Bruzzone, L., Gianelle, D., 2008. Fusion of hyperspectral and LIDAR remote sensing data for classification of complex forest areas. IEEE Trans. Geosci. Remote Sens. 46 (5), 1416–1427.

Dalponte, M., Bruzzone, L., Gianelle, D., 2012. Tree species classification in the Southern Alps based on the fusion of very high geometrical resolution multispectral/hyperspectral images and LiDAR data. Remote Sens. Environ. 123, 258–270.

Douglas, I., 1999. Hydrological investigations of forest disturbance and land cover impacts in South-East Asia: A review. Philos. Trans. R. Soc. London B: Biol. Sci. 354, 1725–1738.

Du, X., Zheng, X., Lu, X., Doudkin, A.A., 2021. Multisource remote sensing data classification with graph fusion network. IEEE Trans. Geosci. Remote Sens. 59 (12), 10062–10072. https://doi.org/10.1109/TGRS.2020.3047130.

Fagan, M.E., Morton, D.C., Cook, B.D., Masek, J., Zhao, F., Nelson, R.F., Huang, C., 2018. Mapping pine plantations in the southeastern US using structural, spectral, and temporal remote sensing data. Remote Sens. Environ. 216, 415–426.

Feng, Q., Yang, J., Zhu, D., Liu, J., Guo, H., Bayartungalag, B., Li, B., 2019a. Integrating multitemporal Sentinel-1/2 data for coastal land cover classification using a multibranch convolutional neural network: A case of the Yellow River Delta. Remote Sens. 11 (9), 1006.

Feng, Q., Zhu, D., Yang, J., Li, B., 2019b. Multisource hyperspectral and lidar data fusion for urban land-use mapping based on a modified two-branch convolutional neural network. ISPRS Int. J. Geo-Inf. 8 (1), 28.

Foody, G.M., 2002. Status of land cover classification accuracy assessment. Remote Sens. Environ. 80 (1), 185–201.

Forzieri, G., Tanteri, L., Moser, G., Catani, F., 2013. Mapping natural and urban environments using airborne multi-sensor ADS40–MIVIS–LiDAR synergies. Int. J. Appl. Earth Obs. Geoinf. 23, 313–323.

Fu, B., Wang, Y., Campbell, A., Li, Y., Zhang, B., Yin, S., Xing, Z., Jin, X., 2017. Comparison of object-based and pixel-based Random Forest algorithm for wetland

vegetation mapping using high spatial resolution GF-1 and SAR data. Ecol. Ind. 73, 105–117.
Furtado, L.F.d.A., Silva, T.S.F., Fernandes, P.J.F., Novo, E.M.L.d.M., 2015. Land cover classification of Lago Grande de Curuai floodplain (Amazon, Brazil) using multi-sensor and image fusion techniques. Acta Amazon. 45 (2), 195–202.
Geerling, G.W., Labrador-Garcia, M., Clevers, J.G.P.W., Ragas, A.M.J., Smits, A.J.M., 2007. Classification of floodplain vegetation by data fusion of spectral (CASI) and LiDAR data. Int. J. Remote Sens. 28 (19), 4263–4284.
Ghamisi, P., Hofle, B., Zhu, X.X., 2017. Hyperspectral and LiDAR data fusion using extinction profiles and deep convolutional neural network. IEEE J. Sel. Top. Appl. Earth Obs. Remote Sens. 10 (6), 3011–3024.
Ghamisi, P., Gloaguen, R., Atkinson, P.M., Benediktsson, J.A., Rasti, B., Yokoya, N., Wang, Q., Hofle, B., Bruzzone, L., Bovolo, F., Chi, M., Anders, K., 2019. Multisource and multitemporal data fusion in remote sensing: A comprehensive review of the state of the art. IEEE Geosci. Remote Sens. Mag. 7 (1), 6–39.
Ghassemian, H., 2016. A review of remote sensing image fusion methods. Information Fusion 32, 75–89.
Guo, L.i., Chehata, N., Mallet, C., Boukir, S., 2011. Relevance of airborne lidar and multispectral image data for urban scene classification using Random Forests. ISPRS J. Photogramm. Remote Sens. 66 (1), 56–66.
Hartling, S., Sagan, V., Sidike, P., Maimaitijiang, M., Carron, J., 2019. Urban tree species classification using a WorldView-2/3 and LiDAR data fusion approach and deep learning. Sensors 19 (6), 1284.
Hasani, H., Samadzadegan, F., Reinartz, P., 2017. A metaheuristic feature-level fusion strategy in classification of urban area using hyperspectral imagery and LiDAR data. European Journal of Remote Sensing 50 (1), 222–236.
Heckel, K., Urban, M., Schratz, P., Mahecha, M.D., Schmullius, C., 2020. Predicting forest cover in distinct ecosystems: The potential of multi-source Sentinel-1 and -2 data fusion. Remote Sens. 12 (2), 302.
Held, A., Ticehurst, C., Lymburner, L., Williams, N., 2003. High resolution mapping of tropical mangrove ecosystems using hyperspectral and radar remote sensing. Int. J. Remote Sens. 24 (13), 2739–2759.
Hofton, M.A., Minster, J.B., Blair, J.B., 2000. Decomposition of laser altimeter waveforms. IEEE Trans. Geosci. Remote Sens. 38 (4), 1989–1996.
Hong, D., Gao, L., Hang, R., Zhang, B., Chanussot, J., 2022. Deep encoder-decoder networks for classification of hyperspectral and LiDAR data. IEEE Geosci. Remote Sens. Lett. 19, 1–5. https://doi.org/10.1109/LGRS.2020.3017414.
Hong, D., Gao, L., Yokoya, N., Yao, J., Chanussot, J., Du, Q., Zhang, B., 2021. More diverse means better: Multimodal deep learning meets remote-sensing imagery classification. IEEE Trans. Geosci. Remote Sens. 59 (5), 4340–4354.
Hribljan, J.A., Suarez, E., Bourgeau-Chavez, L., Endres, S., Lilleskov, E.A., Chimbolema, S., Wayson, C., Serocki, E., Chimner, R.A., 2017. Multidate, multisensor remote sensing reveals high density of carbon-rich mountain peatlands in the páramo of Ecuador. Glob. Change Biol. 23 (12), 5412–5425.
Huang, H., Legarsky, J., Othman, M., 2007. Land-cover classification using Radarsat and Landsat imagery for St. Louis, Missouri. *Photogramm. Eng. Remote Sens.* 73 (1), 37–43.
Huang, W., Sun, G., Dubayah, R., Cook, B., Montesano, P., Ni, W., Zhang, Z., 2013. Mapping biomass change after forest disturbance: Applying LiDAR footprint-derived models at key map scales. Remote Sens. Environ. 134, 319–332.
Hütt, C., Koppe, W., Miao, Y., Bareth, G., 2016. Best accuracy land use/land cover (LULC) classification to derive crop types using multitemporal, multisensor, and multi-polarization SAR satellite images. Remote Sens. 8 (8), 684.
Ienco, D., Interdonato, R., Gaetano, R., Ho Tong Minh, D., 2019. Combining Sentinel-1 and Sentinel-2 satellite image time series for land cover mapping via a multi-source deep learning architecture. ISPRS J. Photogramm. Remote Sens. 158, 11–22.
Iervolino, P., Guida, R., Riccio, D., Rea, R., 2019. A novel multispectral, panchromatic and SAR data fusion for land classification. IEEE J. Sel. Top. Appl. Earth Obs. Remote Sens. 12 (10), 3966–3979.
Inglada, J., Vincent, A., Arias, M., Marais-Sicre, C., 2016. Improved early crop type identification by joint use of high temporal resolution SAR and optical image time series. Remote Sens. 8 (5), 362.
Jahncke, R., Leblon, B., Bush, P., LaRocque, A., 2018. Mapping wetlands in Nova Scotia with multi-beam RADARSAT-2 Polarimetric SAR, optical satellite imagery, and Lidar data. Int. J. Appl. Earth Obs. Geoinf. 68, 139–156.
Jansen, L.J.M., Gregorio, A.D., 2002. Parametric land cover and land-use classifications as tools for environmental change detection. Agric. Ecosyst. Environ. 91 (1-3), 89–100.
Jin, H., Mountrakis, G., Stehman, S.V., 2014. Assessing integration of intensity, polarimetric scattering, interferometric coherence and spatial texture metrics in PALSAR-derived land cover classification. ISPRS J. Photogramm. Remote Sens. 98, 70–84.
Jones, T.G., Coops, N.C., Sharma, T., 2010. Assessing the utility of airborne hyperspectral and LiDAR data for species distribution mapping in the coastal Pacific Northwest, Canada. *Remote Sens. Environ.* 114 (12), 2841–2852.
Ke, Y., Quackenbush, L.J., Im, J., 2010. Synergistic use of QuickBird multispectral imagery and LIDAR data for object-based forest species classification. Remote Sens. Environ. 114 (6), 1141–1154.
Koetz, B., Morsdorf, F., van der Linden, S., Curt, T., Allgöwer, B., 2008. Multi-source land cover classification for forest fire management based on imaging spectrometry and LiDAR data. For. Ecol. Manage. 256 (3), 263–271.
Kuplich, T.M., Freitas, C.C., Soares, J.V., 2000. The study of ERS-1 SAR and Landsat TM synergism for land use classification. Int. J. Remote Sens. 21 (10), 2101–2111.
Kwan, C., Ayhan, B., Budavari, B., Lu, Y., Perez, D., Li, J., Bernabe, S., Plaza, A., 2020a. Deep learning for land cover classification using only a few bands. Remote Sens. 12 (12), 2000.
Kwan, C., Gribben, D., Ayhan, B., Bernabe, S., Plaza, A., Selva, M., 2020b. Improving land cover classification using extended multi-attribute profiles (EMAP) enhanced color, near infrared, and LiDAR data. Remote Sens. 12 (9), 1392.
Laurin, G.V., Liesenberg, V., Chen, Q., Guerriero, L., Del Frate, F., Bartolini, A., Coomes, D., Wilebore, B., Lindsell, J., Valentini, R., 2013. Optical and SAR sensor synergies for forest and land cover mapping in a tropical site in West Africa. Int. J. Appl. Earth Obs. Geoinf. 21, 7–16.
Lee, D.S., Shan, J., 2003. Combining lidar elevation data and IKONOS multispectral imagery for coastal classification mapping. Mar. Geod. 26 (1-2), 117–127.
Li, Y., Ge, C., Sun, W., Peng, J., Du, Q., Wang, K., 2019. Hyperspectral and LiDAR data fusion classification using superpixel segmentation-based local pixel neighborhood preserving embedding. Remote Sens. 11 (5), 550.
Liao, W., Van Coillie, F., Gao, L., Li, L., Zhang, B., Chanussot, J., 2018. Deep learning for fusion of APEX hyperspectral and full-waveform LiDAR remote sensing data for tree species mapping. IEEE Access 6, 68716–68729.
Liu, L., Coops, N.C., Aven, N.W., Pang, Y., 2017. Mapping urban tree species using integrated airborne hyperspectral and LiDAR remote sensing data. Remote Sens. Environ. 200, 170–182.
Lu, D., Li, G., Moran, E., Dutra, L., Batistella, M., 2011. A comparison of multisensor integration methods for land cover classification in the Brazilian Amazon. GIScience Remote Sens. 48 (3), 345–370.
Luo, S., Wang, C., Xi, X., Zeng, H., Li, D., Xia, S., Wang, P., 2016. Fusion of airborne discrete-return LiDAR and hyperspectral data for land cover classification. Remote Sens. 8 (1), 3.
Masek, J.G., Vermote, E.F., Saleous, N.E., Wolfe, R., Hall, F.G., Huemmrich, K.F., Gao, F., Kutler, J., Lim, T.-K., 2006. A Landsat surface reflectance dataset for North America, 1990–2000. IEEE Geosci. Remote Sens. Lett. 3 (1), 68–72.
McNairn, H., Champagne, C., Shang, J., Holmstrom, D., Reichert, G., 2009. Integration of optical and Synthetic Aperture Radar (SAR) imagery for delivering operational annual crop inventories. ISPRS J. Photogramm. Remote Sens. 64 (5), 434–449.
Michelson, D.B., Liljeberg, B.M., Pilesjö, P., 2000. Comparison of algorithms for classifying Swedish landcover using Landsat TM and ERS-1 SAR data. Remote Sens. Environ. 71, 1–15.
Naidoo, L., Cho, M.A., Mathieu, R., Asner, G., 2012. Classification of savanna tree species, in the Greater Kruger National Park region, by integrating hyperspectral and LiDAR data in a Random Forest data mining environment. ISPRS J. Photogramm. Remote Sens. 69, 167–179.
Nyland, R.D., Zipperer, W.C., Hill, D.B., 1986. The development of forest islands in exurban central New York State. Landscape Urban Plann. 13, 111–123.
Pal, M., Mather, P.M., 2003. An assessment of the effectiveness of decision tree methods for land cover classification. Remote Sens. Environ. 86 (4), 554–565.
Park, S., Im, J., Park, S., Yoo, C., Han, H., Rhee, J., 2018. Classification and mapping of paddy rice by combining Landsat and SAR time series data. Remote Sens. 10 (3), 447.
Penner, J.E., 1994. Atmospheric chemistry and air quality. In: Meyer, W.B., Turner, B.L. (Eds.), Changes in Land Use and Land Cover: A Global Perspective. Cambridge University Press, Cambridge, pp. 175–209.
Rasti, B., Ghamisi, P., 2020. Remote sensing image classification using subspace sensor fusion. Information Fusion 64, 121–130.
Reiche, J., Verbesselt, J., Hoekman, D., Herold, M., 2015. Fusing Landsat and SAR time series to detect deforestation in the tropics. Remote Sens. Environ. 156, 276–293.
Sanli, F.B., Kurucu, Y., Esetlili, M.T., 2009. Determining land use changes by radar-optic fused images and monitoring its environmental impacts in Edremit region of western Turkey. Environ. Monit. Assess. 151 (1–4), 45–58.
Sasaki, T., Imanishi, J., Ioki, K., Morimoto, Y., Kitada, K., 2012. Object-based classification of land cover and tree species by integrating airborne LiDAR and high spatial resolution imagery data. Landscape Ecol. Eng. 8 (2), 157–171.
Shupe, S.M., Marsh, S.E., 2004. Cover-and density-based vegetation classifications of the Sonoran Desert using Landsat TM and ERS-1 SAR imagery. Remote Sens. Environ. 93 (1-2), 131–149.
Singh, K.K., Vogler, J.B., Shoemaker, D.A., Meentemeyer, R.K., 2012. LiDAR-Landsat data fusion for large-area assessment of urban land cover: Balancing spatial resolution, data volume and mapping accuracy. ISPRS J. Photogramm. Remote Sens. 74, 110–121.
Skole, D.L., 1994. Data on global land-cover change: Acquisition, assessment and analysis. In: Meyer, W.B., Turner, B.L. (Eds.), Changes in Land Use and Land Cover: A Global Perspective. Cambridge University Press, Cambridge, pp. 437–471.
Sławik, Ł., Niedzielko, J., Kania, A., Piórkowski, H., Kopeć, D., 2019. Multiple flights or single flight instrument fusion of hyperspectral and ALS data? A comparison of their performance for vegetation mapping. Remote Sens. 11 (8), 970.
Song, H., Yang, W., Dai, S., Yuan, H., 2020. Multi-source remote sensing image classification based on two-channel densely connected convolutional networks. Math. Biosci. Eng.: MBE 17 (6), 7353–7377.
Stanton, B.F., Bills, N.L., 1996. The Return of Agricultural Lands to Forest: Changing Land Use in the Twentieth Century. Cornell University, Department of Agricultural, Resource, and Managerial Economics, Ithaca, NY.
Stehman, S.V., 2000. Practical implications of design-based sampling inference for thematic map accuracy assessment. Remote Sens. Environ. 72 (1), 35–45.
Stehman, S.V., 2014. Estimating area and map accuracy for stratified random sampling when the strata are different from the map classes. Int. J. Remote Sens. 35 (13), 4923–4939.
Stehman, S.V., Czaplewski, R.L., 1998. Design and analysis for thematic map accuracy assessment: Fundamental principles. Remote Sens. Environ. 64 (3), 331–344.
Stehman, S.V., Foody, G.M., 2009. Accuracy assessment. In: Warner, T.A., Nellis, M.D., Foody, G.M. (Eds.), The SAGE Handbook of Remote Sensing. Sage Publications, London, pp. 297–309.

Stehman, S.V., Wickham, J.D., Smith, J.H., Yang, L., 2003. Thematic accuracy of the 1992 National Land-Cover Data (NLCD) for the eastern United States: Statistical methodology and regional results. Remote Sens. Environ. 86, 500–516.
Stramondo, S., Bignami, C., Chini, M., Pierdicca, N., Tertulliani, A., 2006. Satellite radar and optical remote sensing for earthquake damage detection: Results from different case studies. Int. J. Remote Sens. 27 (20), 4433–4447.
Sukawattanavijit, C., Chen, J., Zhang, H., 2017. GA-SVM algorithm for improving land-cover classification using SAR and optical remote sensing data. IEEE Geosci. Remote Sens. Lett. 14 (3), 284–288.
Sun, C., Bian, Y., Zhou, T., Pan, J., 2019. Using of multi-source and multi-temporal remote sensing data improves crop-type mapping in the subtropical agriculture region. Sensors 19 (10), 2401.
Sun, G., Ranson, K.J., Guo, Z., Zhang, Z., Montesano, P., Kimes, D., 2011. Forest biomass mapping from lidar and radar synergies. Remote Sens. Environ. 115 (11), 2906–2916.
Teo, T.-A., Huang, C.-H., 2016. Object-based land cover classification using airborne lidar and different spectral images. TAO: Terrest., Atmosph. Ocean. Sci. 27 (4), 491. https://doi.org/10.3319/TAO.2016.01.29.01(ISRS).
Torbick, N., Chowdhury, D., Salas, W., Qi, J., 2017. Monitoring rice agriculture across Myanmar using time series Sentinel-1 assisted by Landsat-8 and PALSAR-2. Remote Sens. 9 (2), 119.
Töyrä, J., Pietroniro, A., Martz, L.W., 2001. Multisensor hydrologic assessment of a freshwater wetland. Remote Sens. Environ. 75 (2), 162–173.
Tucker, C.J., 1979. Red and photographic infrared linear combinations for monitoring vegetation. Remote Sens. Environ. 8 (2), 127–150.
USDA, 2014. 2012 Census of Agriculture: New York: State and County Data. Available online at <https://agcensus.library.cornell.edu/wp-content/uploads/2012-New_York-nyv1-1.pdf≥ (last accessed on January 6, 2021).
USGS, 2020a. Landsat 4-7 Collection 1 (C1) Surface Reflectance (LEDAPS) Product Guide. (Version 3.0). Available online at <https://d9-wret.s3.us-west-2.amazonaws.com/assets/palladium/production/s3fs-public/atoms/files/LSDS-1370_L4-7_C1-SurfaceReflectance-LEDAPS_ProductGuide-v3.pdf> (last accessed on January 6, 2021).
USGS, 2020b. Landsat 4-7 Collection 2 (C2) Level 2 Science Product (L2SP) Guide (Version 3.0). Available online at <https://d9-wret.s3.us-west-2.amazonaws.com/assets/palladium/production/s3fs-public/atoms/files/LSDS-1618_Landsat-4-7_C2-L2-ScienceProductGuide-v3.pdf> (last accessed on January 6, 2021).
van Beijma, S., Comber, A., Lamb, A., 2014. Random forest classification of salt marsh vegetation habitats using quad-polarimetric airborne SAR, elevation and optical RS data. Remote Sens. Environ. 149, 118–129.
Vitousek, P.M., 1994. Beyond global warming: Ecology and global change. Ecology 75, 1861–1876.
Voss, M., Sugumaran, R., 2008. Seasonal effect on tree species classification in an urban environment using hyperspectral data, LiDAR, and an object-oriented approach. Sensors 8 (5), 3020–3036.
Waske, B., Benediktsson, J.A., 2007. Fusion of support vector machines for classification of multisensor data. IEEE Trans. Geosci. Remote Sens. 45 (12), 3858–3866.
Waske, B., van der Linden, S., 2008. Classifying multilevel imagery from SAR and optical sensors by decision fusion. IEEE Trans. Geosci. Remote Sens. 46 (5), 1457–1466.
Wickham, J.D., Stehman, S.V., Smith, J.H., Yang, L., 2004. Thematic accuracy of the 1992 National Land-Cover Data for the western United States. Remote Sens. Environ. 91 (3-4), 452–468.
Wickham, J.D., Stehman, S.V., Fry, J.A., Smith, J.H., Homer, C.G., 2010. Thematic accuracy of the NLCD 2001 land cover for the conterminous United States. Remote Sens. Environ. 114 (6), 1286–1296.
Wickham, J.D., Stehman, S.V., Gass, L., Dewitz, J., Fry, J.A., Wade, T.G., 2013. Accuracy assessment of NLCD 2006 land cover and impervious surface. Remote Sens. Environ. 130, 294–304.
Wickham, J., Stehman, S.V., Gass, L., Dewitz, J.A., Sorenson, D.G., Granneman, B.J., Poss, R.V., Baer, L.A., 2017. Thematic accuracy assessment of the 2011 national land cover database (NLCD). Remote Sens. Environ. 191, 328–341.
Wickham, J., Stehman, S.V., Sorenson, D.G., Gass, L., Dewitz, J.A., 2021. Thematic accuracy assessment of the NLCD 2016 land cover for the conterminous United States. Remote Sens. Environ. 257, 112357. https://doi.org/10.1016/j.rse.2021.112357.
Xu, X., Li, W., Ran, Q., Du, Q., Gao, L., Zhang, B., 2018a. Multisource remote sensing data classification based on convolutional neural network. IEEE Trans. Geosci. Remote Sens. 56 (2), 937–949.
Xu, Z., Guan, K., Casler, N., Peng, B., Wang, S., 2018b. A 3D convolutional neural network method for land cover classification using LiDAR and multi-temporal Landsat imagery. ISPRS J. Photogramm. Remote Sens. 144, 423–434.
Zhang, Y., Zhang, H., Lin, H., 2014. Improving the impervious surface estimation with combined use of optical and SAR remote sensing images. Remote Sens. Environ. 141, 155–167.
Zhou, T., Li, Z., Pan, J., 2018. Multi-feature classification of multi-sensor satellite imagery based on dual-polarimetric Sentinel-1A, Landsat-8 OLI, and Hyperion images for urban land-cover classification. Sensors 18 (2), 373.
Zhu, L., Tateishi, R., 2006. Fusion of multisensor multitemporal satellite data for land cover mapping. Int. J. Remote Sens. 27 (5), 903–918.
Zhu, Z., Woodcock, C.E., Rogan, J., Kellndorfer, J., 2012. Assessment of spectral, polarimetric, temporal, and spatial dimensions for urban and peri-urban land cover classification using Landsat and SAR data. Remote Sens. Environ. 117, 72–82.
Zhuang, W., Mountrakis, G., Wiley, J.J., Beier, C.M., 2015. Estimation of above-ground forest biomass using metrics based on Gaussian decomposition of waveform lidar data. Int. J. Remote Sens. 36 (7), 1871–1889.